ARL

Non-Equilibrium Operation of Long Wavelength HgCdTe Photo Voltaic Detectors for Higher Operating Temperature Applications

by Priyalal S. Wijewarnasuriya

NOTICES

Disclaimers

The findings in this report are not to be construed as an official Department of the Army position unless so designated by other authorized documents.

Citation of manufacturer's or trade names does not constitute an official endorsement or approval of the use thereof.

Destroy this report when it is no longer needed, Do not return it to the originator.

Army Research Laboratory

Adelphi, MD 20783-1197

ARL-TR-6532   **July 2013**

Non-Equilibrium Operation of Long Wavelength HgCdTe Photo Voltaic Detectors for Higher Operating Temperature Applications

Priyalal S. Wijewarnasuriya
Sensors and Electron Devices Directorate, ARL

REPORT DOCUMENTATION PAGE					*Form Approved* *OMB No. 0704-0188*
Public reporting burden for this collection of information is estimated to average 1 hour per response, including the time for reviewing instructions, searching existing data sources, gathering and maintaining the data needed, and completing and reviewing the collection information, Send comments regarding this burden estimate or any other aspect of this collection of information, including suggestions for reducing the burden, to Department of Defense, Washington Headquarters Services, Directorate for Information Operations and Reports (0704-0188), 1215 Jefferson Davis Highway, Suite 1204, Arlington, VA 22202-4302, Respondents should be aware that notwithstanding any other provision of law, no person shall be subject to any penalty for failing to comply with a collection of information if it does not display a currently valid OMB control number. **PLEASE DO NOT RETURN YOUR FORM TO THE ABOVE ADDRESS.**					
1. REPORT DATE *(DD-MM-YYYY)* July 2013		**2. REPORT TYPE** Final		**3. DATES COVERED (From - To)**	
4. TITLE AND SUBTITLE Non-Equilibrium Operation of Long Wavelength HgCdTe Photo Voltaic Detectors for Higher Operating Temperature Applications				**5a. CONTRACT NUMBER**	
				5b. GRANT NUMBER	
				5c. PROGRAM ELEMENT NUMBER	
6. AUTHOR(S) Priyalal S. Wijewarnasuriya				**5d. PROJECT NUMBER**	
				5e. TASK NUMBER	
				5f. WORK UNIT NUMBER	
7. PERFORMING ORGANIZATION NAME(S) AND ADDRESS(ES) U.S. Army Research Laboratory ATTN: RDRL-SEE-I 2800 Powder Mill Road Adelphi, MD 20783-1197				**8. PERFORMING ORGANIZATION REPORT NUMBER** ARL-TR-6532	
9. SPONSORING/MONITORING AGENCY NAME(S) AND ADDRESS(ES)				**10. SPONSOR/MONITOR'S ACRONYM(S)**	
				11. SPONSOR/MONITOR'S REPORT NUMBER(S)	
12. DISTRIBUTION/AVAILABILITY STATEMENT Approved for public release; distribution unlimited.					
13. SUPPLEMENTARY NOTES					
14. ABSTRACT Mercury cadmium telluride (HgCdTe) alloy is of great importance to infrared sensing, and much of the research and development work is carried out for cooled operations. At ambient temperatures, intrinsic carriers are dominant, resulting in high dark currents. This technical report describes ways to reduce intrinsic carriers in ambient temperatures and, in particular, addresses reducing minority carriers in non-equilibrium operation under reverse biases.					
15. SUBJECT TERMS HOT, HgCdTe, non-equilibrium, MBE, P-type, Auger Supprerssion					
16. SECURITY CLASSIFICATION OF:			**17. LIMITATION OF ABSTRACT**	**18. NUMBER OF PAGES**	**19a. NAME OF RESPONSIBLE PERSON** Priyalal S. Wijewarnasuriya
a. REPORT UNCLASSIFIED	**b. ABSTRACT** UNCLASSIFIED	**c. THIS PAGE** UNCLASSIFIED	UU	52	**19b. TELEPHONE NUMBER** *(Include area code)* (301) 394-0963

Contents

List of Figures

List of Tables

Acknowledgment

INTENTIONALLLY LEFT BLANK.

1. Introduction

Mercury cadmium telluride (HgCdTe) alloy is of great importance in sensing radiation from the near infrared ($\lambda_c \sim 1$ µm) to the very long wavelength infrared ($\lambda_c \sim 15$ µm). Much of the HgCdTe-related research and development work is carried out for cooled operation. Intrinsic carriers play a dominant role, especially at long-wavelength (8 µm to 12 µm cut-off) material near ambient temperatures due to high thermal generation of carriers. This results in low minority carrier lifetimes due to high Auger recombination processes. Consequently, this low lifetime at high temperatures results in high dark currents and high noise. Cooling is one means of reducing this type of detector noise. The challenge is to design photon detectors to achieve background-limited performance (BLIP) at the highest possible operating temperature, with the greatest desire being operation close to ambient temperature. Condition of BLIP is defined as the noise being entirely due to the external photon flux and not due to the detector. Hence, BLIP condition depends on the incident photon flux, temperature, detector dark current, etc.

The trick of the trade is to get high-operating-temperature (HOT) detectors, which are being designed to operate at $\sim \Delta T$ K higher temperature than existing detectors, but with performance matching at low temperatures. Another option is to operate these detectors at the same temperature as the existing detectors, but with higher performance.

A higher operating temperature would result in several advantages to an infrared imaging system—mainly a reduction in power and weight requirements, thus lowering mission costs and allowing infrared systems to be deployed on various new platforms. This work would have significant impacts on several mission areas including the Missile Defense Agency, the Army, and other platforms. This technology will increase IR detection range and spatial resolution of imagery, and reduce the carry-on weight of an individual Soldier, and has a significant impact on the size, weight, and power (SWaP) of the overall IR imaging system.

Limiting condition is the existence of high intrinsic carriers near ambient temperatures. Calculated dark current density of a 10 micron cut-off (at 78 K) detector versus temperature is shown in figure 1 together with noise currents calculated for different photon fluxes. As can be seen at 80 K, dark current density is in the range of high 10^6 Amps per cm^2 and exponentially increases as the temperature increases. At 150 K, dark current density is in the low 10^{-2} Amps/cm^2 range. The choice of detector architecture determines the type of dark current that impacts detector performance. Under optimized conditions, dark saturation current density of a state-of-the-art photovoltaic (PV) detector can be written as (see later sections for the derivation),

1

$$J_{0\,diff} = \frac{q n_i^2 d}{N_d \tau_p}$$

where J_{0diff} denotes diffusion current density in the absorber layer, τ_p denotes hole minority carrier lifetime, N_d denotes n-type donor concentration level, n_i denotes the intrinsic carrier concentration, and d is the thickness of the absorber layer.

As shown in figure 1b, the detector is not at BLIP at 100 K for photon flux of less than 10^{15} ph/sec/cm^2 but shows BLIP greater then photon flux of 10^{15}. Hence, dark current suppression is the key to increasing the operating temperature or increasing the performance at a particular temperature. As can be seen from the previous equation, to reduce the dark current, the thickness of the absorber layer and the density of the minority carriers need to be reduced, and/or minority carrier lifetime has to be maximized.
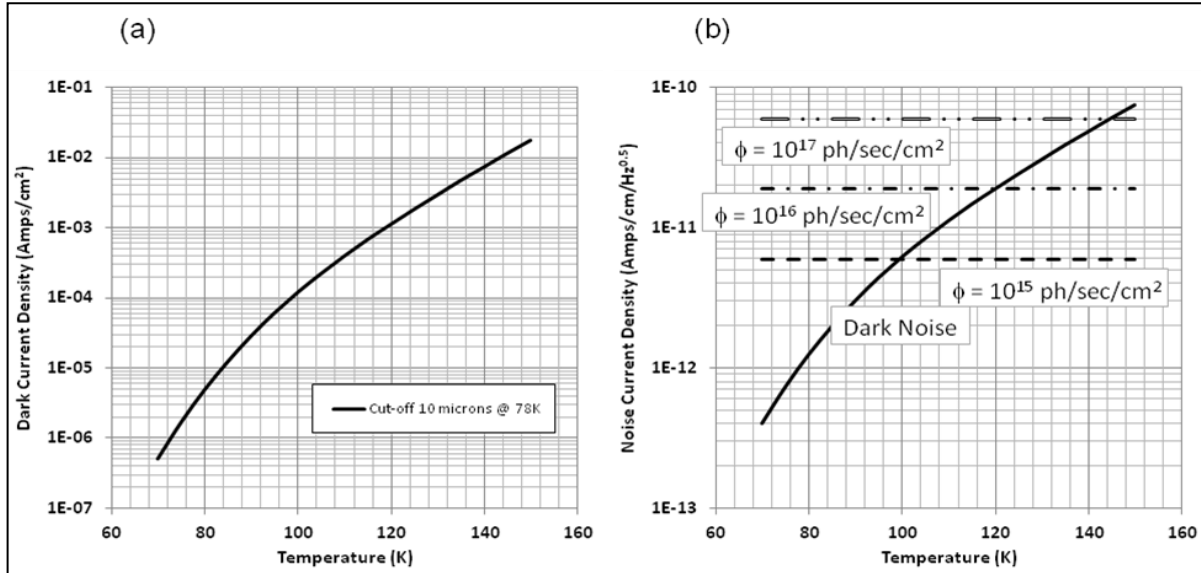
Figure 1. (a) Calculated dark current density versus temperature of a HgCdTe photovoltaic device. Cut-off is 10 microns at 78 K and (b) calculated dark noise and noise due to photon fluxes versus temperature. Noise is in Amps per cm per root Hz.

HOT technology has been untenable because of several severe difficulties in reducing the dark current. The fundamental approach that was used to increase the operating temperature was to reduce the volume of the diffusion region of the device while maintaining the performance at low temperatures. Reducing the diffusion volume of a detector can be achieved by:

a) Reducing the active layer thickness. This approach significantly impacts the absorption of the photons in the long wavelength spectrum of the spectral band pass. When the layer thickness is much less than the cut-off wavelength (dark current is linearly proportional to the absorbing layer thickness), quantum efficiency (QE) at longer wavelengths will suffer drastically. Figure 2

shows an example of such a case (dotted curve). To overcome this problem, one has to have a double pass (or multiple passes), which is a challenge in the device fabrication process.
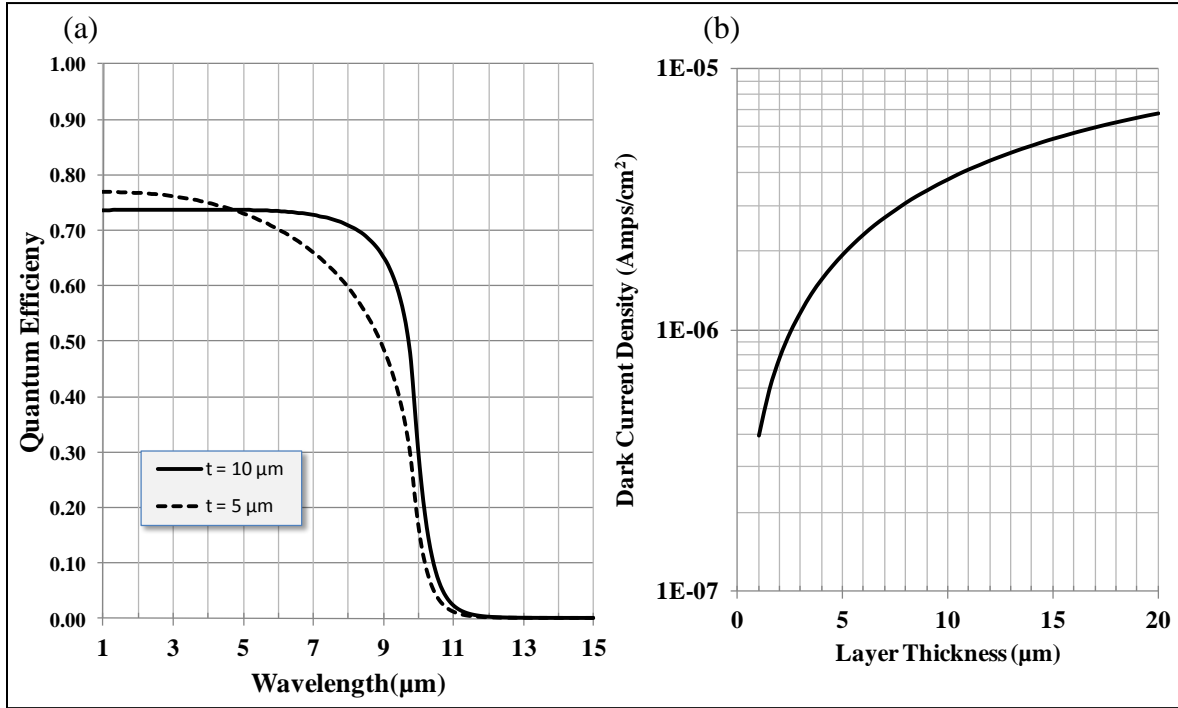
Figure 2. (a) Dependence of absorber thickness on quantum efficiency versus wavelength of a long wave-HgCdTe device (Cut-off (λ_c) is 10 µm) at 78 K. (b. Calculated dark current density versus absorber layer thickness at 78K.

b) Reducing the junction area while maintaining the optical area as the original pixel by using micro-lens technology on a pixel level (*3*) is shown in figure 3. Small junction area will increase the device impedance and, hence, reduce the dark current, thereby reducing the detector Johnson noise and permitting longer integration time for improved signal-to-noise. Additionally, this architecture will reduce the influence of defects intersecting the junction, hence increasing in operability (*4*). One of the challenges is difficulty in producing micro-lenses in a small pitch format on the backside of a substrate.
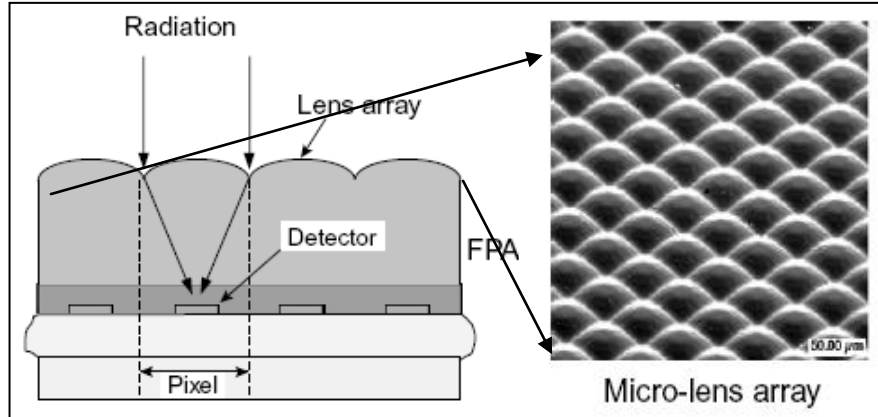
Figure 3. Cross-sectional drawing of micro-lensed hybrid focal plane array of HgCdTe on CdZnTe substrate.

c) Recently, DARPA was soliciting an innovative device architecture inspired by nature (*5*). This is based on a moth-eye nano-pillar-like texture to reduce reflection. Additionally, these pillar-like structures will decrease the diffusion volume of a detector. Hence, photon-trapping device architectures give the same sensitivity as a conventional device, but a much reduced dark current permitting operation in the higher temperatures. The aim of the DARPA program is to demonstrate these nano-pillar structures as an inherent anti-reflection structure (similar to moth-eye) while performing its function as a detector, possibly for HOT applications. One of the issues related to this architecture is the hardness of surface passivation due to high surface to perimeter area (see figure 4).
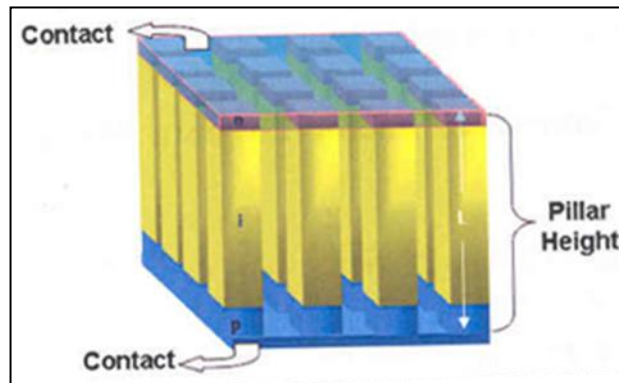
Figure 4. Schematic example of a one pixel pillar like structure with 16 sub-element.

As explained earlier, besides reducing the diffusion volume, other methods of reducing the dark currents are:

4

1) Increasing the minority carrier lifetime, and

2) Reducing the minority carrier concentration.

This report will henceforth describe these two methods of reducing dark currents of a given PV device.

The dominant intrinsic recombination mechanism in long-wavelength HgCdTe is Auger recombination. The electron-initiated Auger-1 process dominates in n-type material, whereas the hole-initiated Auger-7 process dominates in p-type material. Intrinsic Auger-7 lifetimes are significantly longer than intrinsic Auger-1 lifetimes (*1, 2*). Hence, p-type HgCdTe absorber material is preferred for higher operating temperature application devices (*2*).

2. Nonequilibrium Mode of Operation–Auger Suppression

Recently, Ashley and Elliott (*6–8*) proposed a new class of infrared sensing devices that used the phenomena of exclusion and extraction of thermally generated carriers from the active region under reverse bias, thereby suppressing Auger processes. I will be discussing device architecture, which relates to exclusion and extraction junction in HgCdTe $\underline{P}^+$/p/$\underline{N}^+$ configuration. Similar work was done by Elliot (*6*) in indium antimony (InSb) material system. In this report, I am discussing a $\underline{P}^+$/π/$\underline{N}^+$ HgCdTe structure, where the symbol ''π'' indicates a drastically reduced extrinsic p-type carrier concentration in the order of mid 10^{15} cm^{-3}; $\underline{P}^+$ and $\underline{N}^+$ denote higher doping density, as well as a higher energy gap than the photosensitive base p-region. In the π-region, the minority carriers are electrons. When the minority carriers are electrons, a gain of approximately 60 times in the minority carrier lifetime is obtained (see figure 8) because of the lack of symmetry between the valence and conduction bands in LW-HgCdTe, regardless of doping.

The challenge to this approach is to obtain low p-type doping levels in the π-region in HgCdTe material grown by molecular beam epitaxy (MBE). Such a low level of p-type doping has never been demonstrated in a controlled manner by MBE for HgCdTe (*9–11*). The goal of obtaining a reduced p-type carrier concentration will be to reduce the Auger generation-recombination carrier dynamics and to provide the enhanced carrier diffusion required for high quantum efficiency and low dark currents, resulting in enhanced D*.

The typical device structure is shown in figure 6. The intrinsic carrier concentration in Hg$_{0.78}$Cd$_{0.22}$Te is increases as the temperature is increased (see figure 5). It can reach values as high as 10^{16} cm^{-3} near ambient temperatures, i.e. values higher than the actual extrinsic doping level. Therefore, since Auger processes are directly proportional to the number of electrons and holes available, it will result in high dark currents in HgCdTe IR devices operated at high

temperatures where the absorber layer is intrinsic at equilibrium. The $\underline{P}^+/\pi$ heterojunction is referred to as the exclusion junction (see figure 6). The $\pi/\underline{N}^+$ heterojunction is referred to as the extraction junction. For example, consider a $\underline{P}^+/\pi/\underline{N}^+$ structure operated at high temperature so that the 'π' absorber region is intrinsic in thermal equilibrium. As an example at 200 K, the intrinsic carrier concentration is in the mid-10^{15} cm^{-3} for Hg$_{0.78}$Cd$_{0.22}$Te material (see table 1). Applying an increasing reverse bias to the device, the $\pi/\underline{N}^+$ extraction junction extracts the minority electrons from the 'π' absorber region faster than they can be injected from the $\underline{P}^+/\pi$ interface region. One of the conditions is that the diffusion length of electrons in the $\underline{P}^+$ region should be less than the thickness of $\underline{P}^+$ region, and the diffusion length of the electrons in the 'π' absorber region should be greater than the thickness of the 'π' absorber region. This condition will not allow electrons in the $\underline{P}^+$ region to cross over to the 'π' absorber region. Since in the $\underline{P}^+$ region electron concentration, diffusion length of electrons is very low (see the table), electrons cannot be replenished to the 'π' absorber region. Therefore, the electron concentration drops significantly, below its thermal equilibrium value, in the 'π' absorber region. Higher band gap in the $\underline{P}^+$ region help this process, as well as an electron barrier in between $\underline{P}^+$ region and 'π' absorber region. The hole concentration is also reduced below the equilibrium value in order to maintain charge neutrality. As the reverse bias is increased, the electron concentration in the absorber region will eventually go from the intrinsic level (mid-10^{15} cm^{-3}) down to the extrinsic doping levels, as shown in figure 5 and table 1. This decrease of electron concentration in the absorber region by several orders of magnitude as the reverse bias is increased results in significant reduction of Auger processes and, hence, reduction in dark current at ambient temperatures. Figure 7 illustrates calculated electron and hole concentration in the three regions (see figure 6) at 300 K.

Auger suppression in HOT HgCdTe devices translates into a unique negative differential resistance (NDR) in the reverse bias current-voltage (I-V) characteristics, which has been experimentally observed in devices grown by MOVPE (*6*) and MBE using silver as an acceptor dopant (*12*). More recently, Wijewarnasuriya et al (2008) reported Auger suppression in LWIR MBE-grown devices using arsenic as an acceptor dopant (*13*).
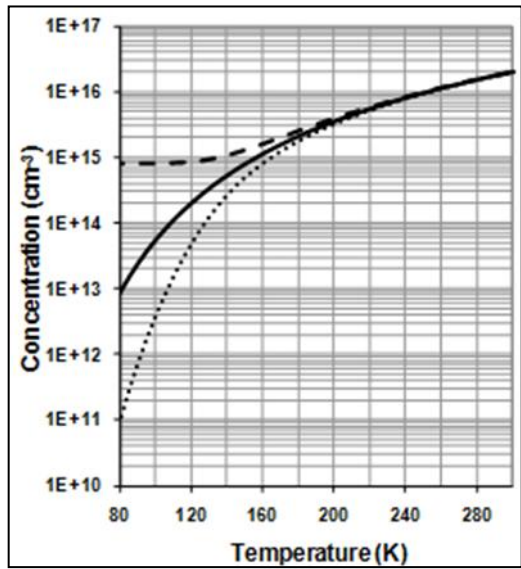
Figure 5. Temperature dependence of intrinsic
(solid line), electron (dash line) and hole
(dotted line) concentration versus temperature
of n-type $Hg_{0.78}Cd_{0.22}Te$ material.
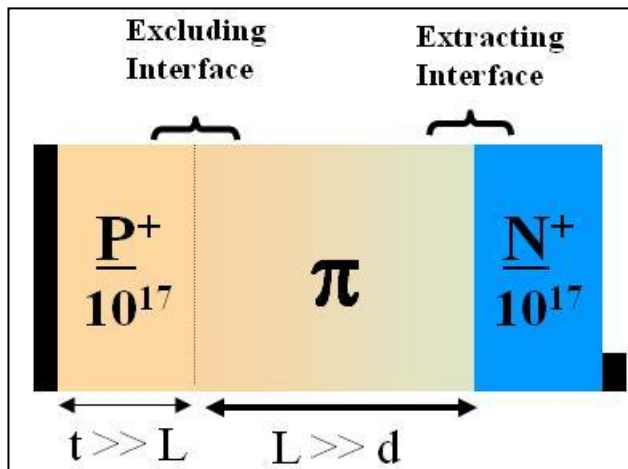
Figure 6. HgCdTe HOT infrared photodiode structure; "t" is
the $\underline{P}^+$ layer thickness, "d" is the π-layer thickness,
and "L" is the diffusion length of electrons in the
respective $\underline{P}^+$ and π-layers.

Table 1. Calculated intrinsic, hole, and electron concentration in the individual layers of $\underline{P}^+/\pi/\underline{N}^+$ structure at 78 K and at 200 K.

Layer	$\underline{P}^+$	π	$\underline{N}^+$	$\underline{P}^+$	π	$\underline{N}^+$
X	0.3	0.225	0.3	0.3	0.225	0.3
	at 78K			at 200K		
n_i (cm^{-3})	1.50E+09	**7.00E+12**	1.50E+09	1.00E+14	**3.50E+15**	1.00E+14
p_0 (cm^{-3})	1.00E+17	**1.00E+15**	2.25E+01	1.00E+17	**4.00E+15**	4.00E+11
n_0 (cm^{-3})	2.25E+01	**5.00E+10**	1.00E+17	4.00E+11	**3.00E+15**	1.00E+17
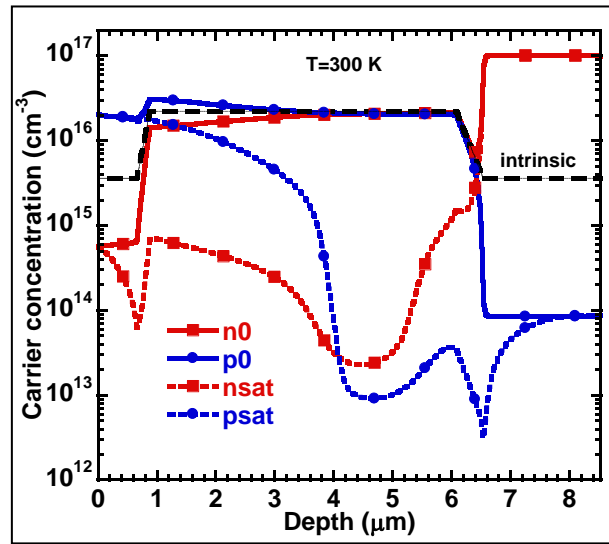
Figure 7. Calculated electron and hole concentration in the three layers (see figure 6) of a LWIR HOT structure at 1 V reverse bias. Also indicated is the doping levels.

3.   Carrier Recombination Mechanisms in HgCdTe

As described earlier, one way to reduce dark current is to increase the minority carrier lifetime. Let us look at the carrier lifetime mechanisms in HgCdTe. Minority carrier lifetime in n-type HgCdTe is determined by several different recombination mechanisms, discussed extensively in the literature (*14–27*). In particular, Auger, radiative, and Shockley-Read-Hall (SRH) processes are important recombination mechanisms in HgCdTe. The first two—Auger and radiative mechanisms—are fundamental to the material, while the last is initiated by defects that may be eliminated through high quality material growth and device processing advances.

The Auger-1 process (*24*) is the dominant recombination mechanism in n-type material. In this mechanism, an excited electron in the conduction band recombines with a hole in the valence band, and the loss in energy is transferred to a second conduction-band electron by the electron-electron coulomb interaction. Overall, this involves two electrons and a heavy hole. Under low injection conditions, lifetime for Auger-1 limited recombination has been described in terms of (*14*),

$$\tau_{A1} = \frac{2n_i^2 \tau_{Ai}}{(n_0 + p_0)(n_0 + \xi p_0)} \ ,$$

where, n_i is the intrinsic carrier concentration, n_0, p_0 are equilibrium electron, hole concentration, and τ_{Ai} is the Auger lifetime for intrinsic HgCdTe and ξ is the hole-hole collision term, which we have neglected for HgCdTe. τ_{Ai} is given by (*14–16, 19*)

$$\tau_{Ai} = \frac{3.8 \times 10^{-18} \varepsilon^2 (1+\eta)^{1/2} (1+\eta)}{(m_e^*/m_0)|F_1 F_2|^2 (kT/E_g)^{3/2}} \times \exp\left(\frac{(1+2\eta)}{(1+\eta)} \frac{E_g}{kT}\right) \ ,$$

giving τ_{Ai} in seconds. In this last expression, k is Boltzmann's constant and T is the absolute temperature, E_g is the gap energy (*28*), and ε is the dielectric constant, given in (*15*) to be 20 – 9.4x. Also, m_0 is the electron rest mass, m^*_e and m^*_h are electron and hole-effective masses, and $\eta = m^*_e/m^*_h$. The value for $|F_1 F_2|$ typically varies between 0.1 and 0.3 (*15–23*). The best way is to get $|F_1 F_2|$ empirically is to study the concentration dependence of lifetimes at 78 K since there exits ambiguity in the exact value of $|F_1 F_2|$ in the literature. Figure 8 shows the lifetime behavior versus electron concentration of n-type doped HgCdTe at 78 K for X=0.22. The lifetime data follows extremely well for doping levels above 10^{15} cm^{-3} for $|F_1 F_2| = 0.18$.

In p-type material in addition to the Auger-1 process, the Auger-7 process (*24, 28*) is also important. In this process, an excited electron in the conduction band recombines with a hole in the valance band and the loss in energy is transferred to an electron in the light hole band. Under low injection conditions, Auger-7 lifetime in p-type material is given by (*19, 22*),

$$\tau_{A7} = \frac{2n_i^2 \gamma \tau_{A1}}{(n_0 + p_0)p_0},$$

where, the ratio $\gamma = \tau_{A7}/\tau_{A1}$ has been calculated in (*28*).

9
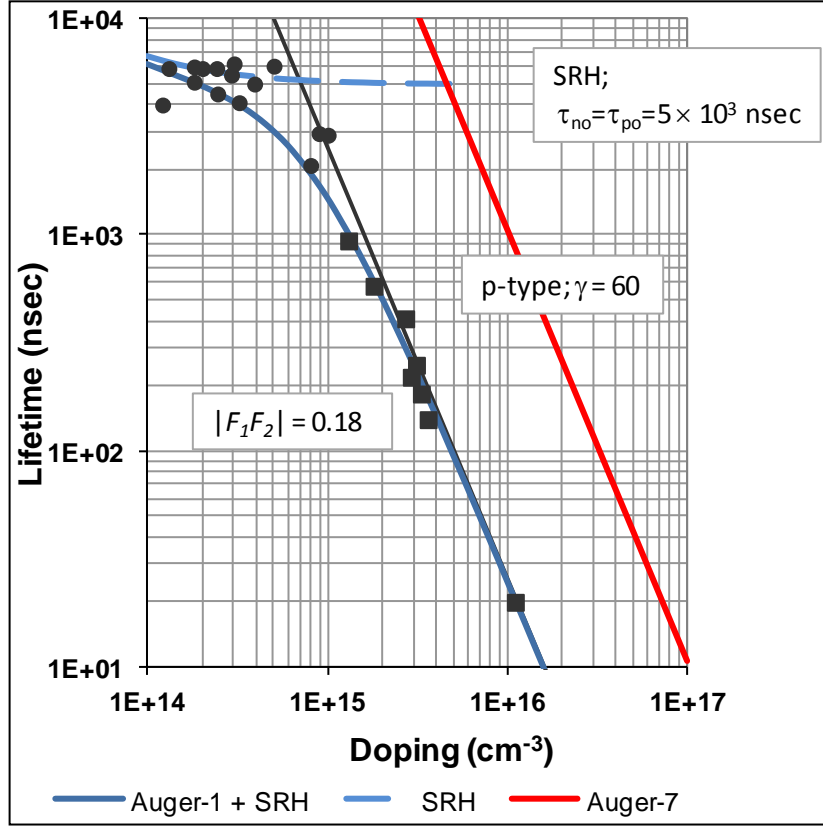
Figure 8. The dependence of minority carrier lifetime on electron density at 78 K
on indium-doped MBE-grown HgCdTe layers. Lines show varies contributions;
dashed-line – SR recombination and red solid line for p-type HgCdTe which shows
much higher expected electron lifetime.

At this time, there is no clear agreement for γ in HgCdTe which is related to the magnitude of Auger-7 processes. Consequently, we set $\gamma = 60$ in this study which is the most common value used.

Next, radiative recombination lifetime has been described in terms of (*15, 16, 19*)

$$\tau_R = \frac{1}{B(n_0 + p_0)},$$

with *B* being given by

$$B = 5.8 \times 10^{-13} \varepsilon^{1/2} \left(\frac{m_0}{m_e^* + m_h^*} \right) \left(1 + \frac{m_0}{m_e^*} + \frac{m_0}{m_h^*} \right) \times \left(\frac{300}{T} \right)^{3/2} \left(E_g^2 + 3kTE_g + 3.75k^2T^2 \right),$$

giving τ_R in seconds. The recombination of electron-hole pairs occurs between conduction and valence bands, and the excess energy is released in the form of photons.

Finally, Shockley-Read lifetime, assuming a single recombination level E_t below the conduction band edge, and low injection levels, has been described in terms of (*14, 19, 27*),

$$\tau_{SR} = \frac{\tau_{p0}(n_0 + n_1)}{n_0 + p_0} + \frac{\tau_{n0}(p_0 + p_1)}{n_0 + p_0},$$

where, τ_{n0} and τ_{p0} denote shortest-time constant values for electron and hole capture, respectively, $n_1 = n_0 \exp[(E_t - E_F)/kT]$, $p_1 = p_0 \exp[(E_F - E_t)/kT]$, and E_F denotes the Fermi energy.

As can be seen from figure 8, for low level of doping concentrations (less than 10^{15} cm^{-3}) in n-type material, SRH lifetime is necessary in addition to band-to-band recombination to explain the data. Data explain very well with $\tau_{n0} = \tau_{p0} = 5$ μsec for LW n-type materials doped with indium. This agrees very well with data obtained in LPE materials, as well (*2*).

When the lifetime is not dominated by a single process, it is necessary to calculate the lifetime accordingly. Thus, if all three recombination mechanisms are important, the overall effective lifetime τ is then calculated from,

$$\frac{1}{\tau} = \frac{1}{\tau_A} + \frac{1}{\tau_R} + \frac{1}{\tau_{SR}},$$

where τ_A, τ_R, and τ_{SR} are the Auger, radiative and SRH lifetimes, respectively.

4. Current Mechanisms in a Photo Voltaic Junction

The choice of PV detector architecture determines the type of dark currents that impact detector performance, and ultimately, determine the signal-to-noise ratio. Currents from the n-side active layer should only limit high-quality $\underline{P}^+$/n devices operating in the diffusion-limited region. In a proper design of a detector, the active layer thickness **d** is less than the diffusion length of the minority carriers. Dark diffusion current of a PV detector can be expressed as follows (*29*):

$$I_{Diff} = I_{0Diff}\left[\exp\left(\frac{qV}{nkT}\right) - 1\right],$$

where q is the electron charge, k is Boltzmann's constant, T is absolute temperature, n is the ideality factor equals to 1, V is the bias voltage across the diode, and J_{0Diff} is the saturation diffusion current density.

Diffusion current contributions to reverse saturation current J_{0Diff} consist of components from p and n-sides of the junction, expressed here in current density superposition form as (*30–33*)

$$J_{0\,diff} = qn_i^2 \left[\frac{L_p}{N_d \tau_p} + \frac{L_n}{N_a \tau_n} \right]$$

where J_{0diff} denotes diffusion current density, $L_{p,n}$ and $\tau_{p,n}$ denote minority diffusion lengths and lifetimes on respective n and p sides of the junction , and $N_{d,a}$ denote donor and acceptor concentration levels on the n and p sides of the junction. For the case of p-on-n double heterostructures where the p-side has a wider bandgap and high doping N^+_a, the second term in $J_{0\,diff}$ is negligible compared to the first and J_{0diff} reduces to

$$J_{0\,diff} = \frac{qn_i^2 L_p}{N_d \tau_p}$$

When the n-type active (absorber) layer thickness d is smaller than the diffusion length L_p, dimension d effectively replaces L_p to give

$$J_{0\,diff} = \frac{qn_i^2 d}{N_d \tau_p}$$

Second important current mechanism is the generation-recombination (g-r) current density which arises due to imperfections in the space charge region.

Early treatments developed the seminal formulation for g-r phenomena in semiconductor junctions (*34*). Phenomenologically, electron-hole pairs generated thermally in the depletion region give rise to a current that is recombination-behaving under forward bias and generation-behaving under reverse bias. Derivations for this current historically take the form;

$$J_{g-r} = \frac{qn_i W}{\sqrt{\tau_{n0} \tau_{p0}}} \frac{Sinh\left(\frac{qV}{2kT}\right)}{q\left[\frac{(V_{bi} - V)}{2kT}\right]} f(b)$$

where,

$$f(b) = \int_0^\infty \frac{du}{u^2 + 2bu + 1} \ , \qquad b = e^{-qV/2kT} \cosh\left[\frac{E_t - E_i}{kT} + \frac{1}{2}\ln\left(\frac{\tau_{p0}}{\tau_{n0}}\right)\right]$$

Trap levels due to defects are most effective when they exist close to the intrinsic Fermi level, i.e., when $E_t = E_i$. For bias conditions where $V \approx 0$, along with assumptions that $E_t = E_i$ and $\tau_{po} = \tau_{no} = \tau_o$, it follows that $b \approx 1$ and $f(b) \approx 1$. Under these provisos, $J_{g\text{-}r}$ reduces to

$$J_{g\text{-}r} = \frac{qn_iW}{\tau_o}\frac{2kT}{q(V_{bi} - V)}\sinh\left(\frac{qV}{2kT}\right).$$

Generation-recombination current $J_{g\text{-}r}$ current is seen to be proportional to n_i. As such, generation-recombination $J_{g\text{-}r}$ current will tend to dominate over diffusion J_{diff} current at low temperatures.

From the previous equation, g-r current arises due to imperfections in the space charge region and takes the form of

$$I_{g\text{-}r} = I_{og\text{-}r}\sqrt{V_{bi} - V}\left[\exp\left(\frac{qV}{nkT}\right) - 1\right],$$

where $I_{og\text{-}r}$ is the g-r saturation current (which is a fitting parameter) and n is the ideality factor equal to 2.

Tunneling currents can dominate in narrow-band gap HgCdTe devices at low temperatures, where thermally generated currents are low, and this is the dominant current mechanism under reverse biases under such conditions. Tunneling currents come in two forms, namely, (1) band-to-band (BTB) and (2) trap-assisted tunneling (TAT), where forbidden gap energy states promote and participate in a two-step process. BTB tunneling currents result in electrons tunneling directly from the valance band to the conduction band and are given by (*35*)

$$I_{BTB} = \frac{Aq^3EV}{4\pi^2\hbar^2}\sqrt{\frac{2m^*}{E_g}} * \left[\exp\left(-\frac{4\sqrt{2m^*}E_g^{1.5}}{3qE\hbar}\right)\right] * \left[1 - \exp\left(\frac{qV}{kT}\right)\right],$$

where A is the junction area, E is the electric field, $\hbar$ is the reduced Planck constant, m^* is the tunneling effective mass, and E_g is the band gap. These currents are due to direct tunnelling of carriers under relatively high reverse biases. These currents are fairly independent of temperature, and calculated BTB currents at 78 K for a band gap of 115 meV is insignificant.

TAT current (I_{TAT}) arises from electrons transitioning from the valence band to a trap level within the forbidden gap and then tunneling to the conduction band. The current density is given by (*36*)

$$I_{TAT} = \frac{A\pi^2 q^2 m^* E M^2 N_t W}{\hbar^3 (E_g - E_t)} \sqrt{\frac{2m^*}{E_g}} * \left[\exp\left(-\frac{\sqrt{m^*/2}\, E_g^{1.5} F(a)}{2qE\hbar} \right) \right] * \left[1 - \exp\left(\frac{qV}{kT} \right) \right],$$

where M is the transition matrix element, N_t is the trap density in cm^{-3}, E_t is the trap energy, and F(a) is function of E_t/E_g.

Finally, currents due to shunting (I_{SH}) across the diode are given by

$$I_{SH} = \frac{V}{R_{SH}},$$

where R_{SH} is the shunt resistance. Usually, surface leakage currents and shunt currents are due to the intersection of dislocation, defects, etc., which are possible sources of this category of excess currents.

Combining the previously mentioned considerations relative to diffusion, g-r, BTB, TAT, and shunt currents, detector overall dark current is given by

$$I_{Total} = I_{Diff} + I_{g-r} + I_{BTB} + I_{TAT} + I_{SH}.$$

Figures 9 and 10 compare the measured versus modeled I-Vs from the previous equations for two $\underline{P}^+$/n HgCdTe PV devices. The model calculates ideal diffusion currents from the active region from the measured material parameters, such as doping N_d, active layer thickness d, and λ_c at 78 K. The measured λ_c at 78 K is 10.0 μm. Diffusion currents from the n-type active region fit very well down to −0.05 V, indicating that the dominant current mechanism is diffusion close to zero bias and a diffusion current of 3.18×10^{-10} A was measured. At larger biases (greater than −0.4 V), the measured currents were significantly higher than the diffusion currents, and our model calculation shows that these are due to TAT (dotted line). The solid line in figure 9 is the contribution of diffusion, TAT, and shunt currents. The BTB and g-r current contributions were negligible. A very good agreement exists between the measured and model calculations, as can be seen from figure 9. As evidenced by the R_d versus V curve, there is a slight shunt current contribution between the −300 and −50 mV region. Shunt resistance is 5×10^9 Ω. Close to zero bias, the obtained shunt resistance is much higher than the diode impedance and, hence, has no effect on zero bias impedance (R_oA) on "good devices." On the other hand, figure 10 compares the measured versus calculated I–Vs for another diode. In contrast to the previous diode, a flat reverse saturation current is not seen close to zero bias. The reverse current linearly increases as the bias voltage increases, and ultimately, at larger biases, TAT currents dominate. In order to get a good fit to the measured I–V data, a shunt current plus TAT current are needed in addition to the diffusion current. Currents are diffusion at zero bias, but a slight reverse bias shows a deviation from this current mechanism. Instead, measured

currents close to, but not at, zero biases exhibit a shunt behavior and shunt resistance of $7.8 \cdot 10^7 \, \Omega$, which have been assumed in order to get a good fit to the measured data.
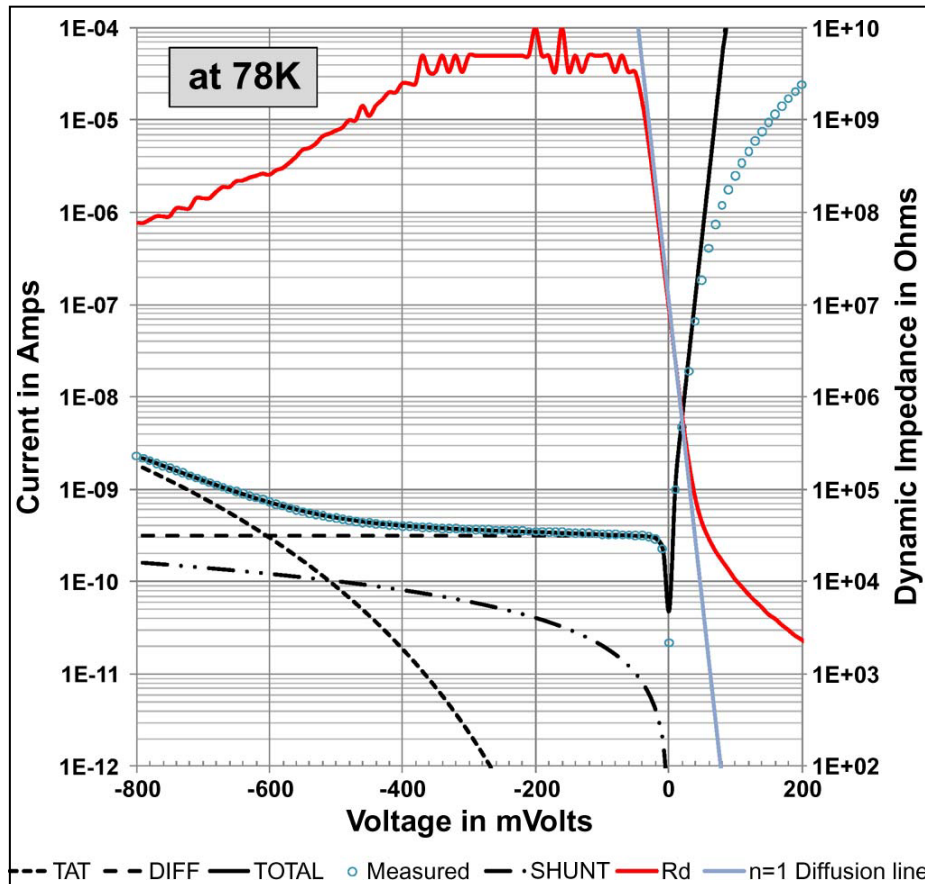
Figure 9. Dependence of measured (symbols) and modeled (lines) of current versus bias voltage at 78 K. The total current (solid line) is modeled with a diffusion saturation current of 3.18×10^{-10} Amps along with trap-assisted tunneling and shunt currents. A shunt resistance of $5 \times 10^9 \, \Omega$ is assumed in the model calculation.

The dashed line in figure 10 with $n = 1$ matches the R_d versus voltage curve, further confirming that the dominant current mechanism is diffusion.

The lowest dark current is achieved when radiative recombination is dominant. The radiative recombination process has been found to be a non-issue in near-equilibrium situations and can be ignored due to photon recycling (2, 37). This leaves generation currents from the SRH centers as the major source of leakage currents limiting performance, even at ambient temperatures. Hence, the ultimate limitation is the Auger recombination and, if suppressed, this will lead closer to background-limited directivity D* at ambient temperatures on good-quality p-type absorber materials. Figure 11 shows the calculated saturation dark current density versus temperature for $\lambda_{co} = 10 \, \mu m$ photovoltaic devices at 100 K for a doping density of $2.0 \times 10^{15} \, cm^{-3}$. The Cd composition is 0.22. The PV device designs under consideration are double-layer heterostructure

$\underline{P}^+/n$, $\underline{N}^+/p$, and $\underline{P}^+/\pi/\underline{N}^+$ under high reverse-bias operation. As shown in the figure, high dark current dominates at operation near ambient temperature in $\underline{P}^+/n$ structures due to high Auger recombination in n-type materials. This dark current could be decreased in $\underline{N}^+/p$ devices due to higher minority Auger carrier lifetimes (factor of γ) than n-type absorber layers. This dark current could be suppressed even further by the phenomena of exclusion and extraction in $\underline{P}^+/\pi/\underline{N}^+$ devices, as indicated in the figure. The phenomena of minority carrier exclusion and extraction under high biases have been described previously (*1, 6–8*). In the $\underline{P}^+/\pi/\underline{N}^+$ device architecture, the π-region is the absorbing layer. At ambient temperatures, the minority and majority carrier concentrations in the p-region are approximately equal and, hence, behave as near intrinsic (see table 1). This will give high dark current, and, therefore, noise, due to dominating intrinsic carriers.
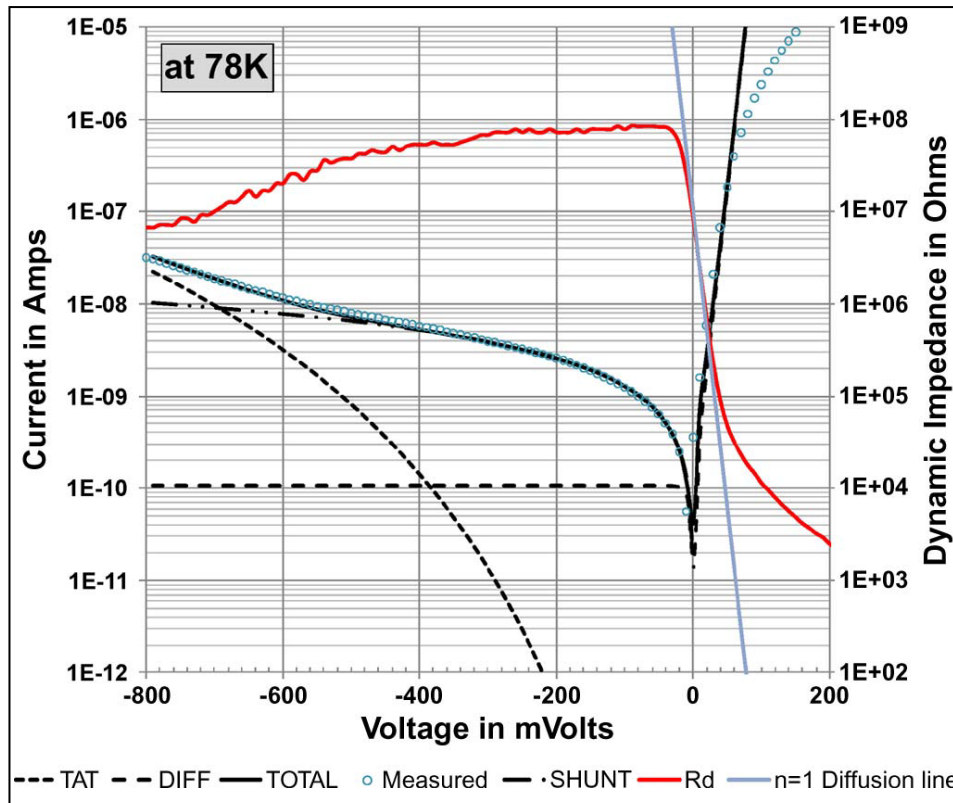

Figure 10. Dependence of measured (symbols) and modeled (lines) of current versus bias voltage of a diode at 78 K. The total current (solid line) is modeled with diffusion saturation current of 1.08×10^{-10} Amps along with trap assisted tunneling and shunts currents. A shunt resistance of 7.8×10^7 Ω is assumed.

Trick is to reduce the minority carrier concentration—as an example at 200 K, from 3×10^{16} cm^{-3} to concentration levels of 3×10^{15} cm^{-3} at 78 K.

The concept is to reduce both minority and majority carrier concentrations from their equilibrium value to the levels of extrinsic conditions so that extrinsic behavior will be observed at ambient

temperatures (*6–8*). These reduced carriers will give suppressed Auger recombination lifetimes. Figure 11 shows the dark current density versus temperature on such a $\underline{P}^+/\pi/\underline{N}^+$ device architecture under exclusion and extraction. As can be seen, this device architecture gives the lowest dark current densities as ambient temperatures are approached, which gives the potential to yield closer to BLIP operation. Further, if very low levels of p-type acceptor concentrations ($N_a \sim 10^{14}$ cm^{-3}) can be achieved, then near-BLIP operation at ambient temperature should be possible. The photocurrent due to 300 K blackbody radiation is 4×10^{-5} A for a quantum efficiency of unity. As Elliott and co-workers have pointed out, one of the main limitations of this structure is the leakage of electrons from the $\underline{P}^+$ to the p-region close to ambient temperatures. A slightly modified structure has been proposed to surmount this situation (*38*). In this report, we discuss the results of $\underline{P}^+/\pi/\underline{N}^+$ device structures grown by MBE.
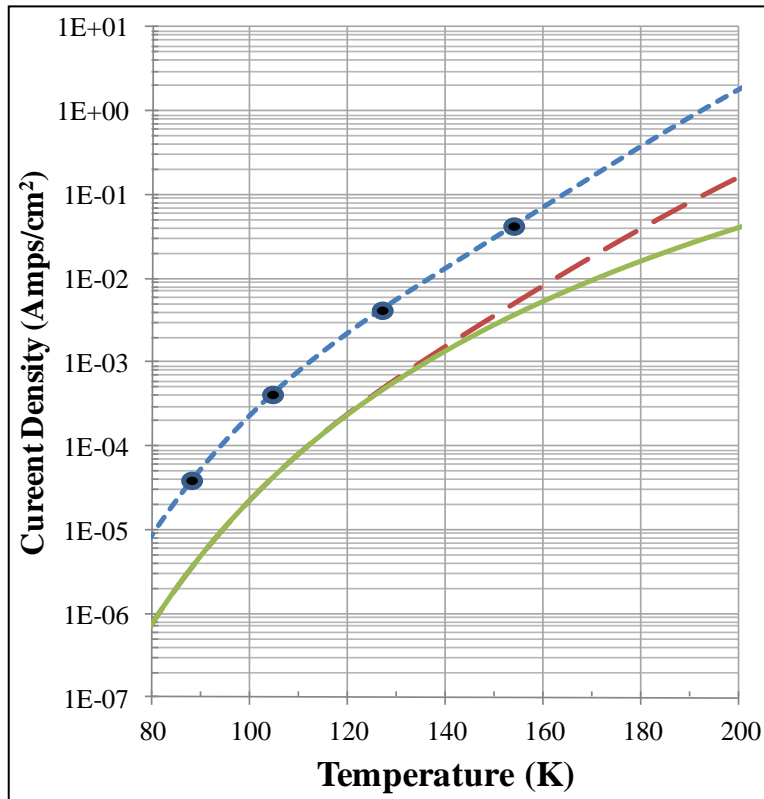
Figure 11. Calculated dark current density versus temperature: (a) for $\underline{P}^+/n$ device (dotted line), (b) for $\underline{N}^+/p$ (dash line), and (c) $\underline{P}^+/\pi/\underline{N}^+$ (solid line) under high reverse-bias operation. The calculation assumes a one-dimensional (1-D) device model, currents only from active absorber layers, and active absorber doping concentrations of 2×10^{15} cm^{-3}. For comparison purposes, the photocurrent due to 300 K blackbody radiation is 4×10^{-5} Amps for a quantum efficiency of unity.

5. Experiment

5.1   MBE Growth of HgCdTe

Layers characterized here were grown by MBE on (211)B CdZnTe substrates. Figure 12 shows a schematic cross section of the $\underline{P}^+/\pi/\underline{N}^+$ planar detector architecture. The key feature of the detector architecture is the planar device geometry, with a narrow-bandgap active p-layer sandwiched between a wide-band $\underline{P}^+$ cap layer and a wide-band $\underline{N}^+$ layer. Benefits of this architecture include a buried narrow-bandgap active layer, resulting in a reduction in surface generation-recombination and surface tunneling currents, and an inherent ease to passivate the wider-band gap cap layer (*39, 40*). $\underline{P}^+$ indicates higher Cd composition as well as higher p-type doping than the base layer and $\underline{N}^+$ indicates higher Cd composition, as well as higher n-type doping than the base layer. All three regions shown in figure 12 are *in-situ* indium-doped during the MBE growth, and the doping levels are shown in the table in the figure. Arsenic-ion implantation was performed in selected regions followed by a deep diffusion plus activation anneal to fabricate $\underline{P}^+/\pi/\underline{N}^+$ detectors as a planar configuration into process evaluation chips (PEC) containing devices with variable areas.

Region	as-grown				After Implant + Anneal	
	Thickness (μm)	Cd	Doping (cm^{-3})	Type	Doping (cm^{-3})	Type
I	2.0	0.30	1.0×10^{17}	N$^+$	1.0×10^{17}	N$^+$
II	5.2	0.22	1.0×10^{15}	n	Mid x10^{15}	π –graded
III	0.9	0.30	1.0×10^{15}	N	Low x10^{16}	P$^+$
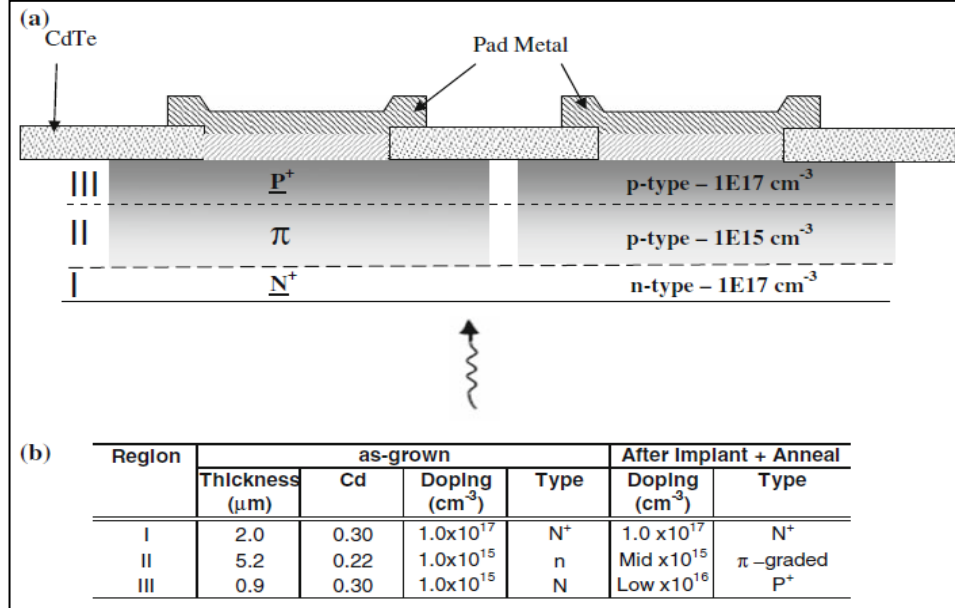
Figure 12. (a) Cross section of the $\underline{P}^+/\pi/\underline{N}^+$ planar device architecture grown by molecular beam epitaxy. Implantation plus a diffusion process were used to obtain p-absorber layer.
(b) Table of material characteristics of the different regions of the device structure before and after implantation/diffusion anneal.

We mainly concentrated on 250-μm-diameter devices in this report. These fabricated devices were then characterized electrically and optically down to 78 K from 300 K. Backside illumination was used for all optical measurements. The spectral response was measured with a Fourier transform infrared (FTIR) spectrometer, and the 50% spectral response point was taken as the cut-off wavelength of the device.

5.2 Low Arsenic Doping in HgCdTe - π Absorber Region

In this work, arsenic was used as a source of extrinsic p-type carriers with the proper arsenic doping level obtained by a novel diffusion technique based on diffusion by thermal annealing to obtain $\underline{P}^+/\pi$ region in the planar devices architecture in MBE-grown n-type HgCdTe layers.

In early work (*12*), Auger suppression in MBE-grown HgCdTe heterostructure devices using silver (Ag) as a p-type doping was demonstrated. However, the use of group V elements as p-type dopants in MBE has been studied extensively due to the larger atomic size of the group V elements and, hence, their lower diffusivity in HgCdTe. This fact allows for stable and well-controlled p–n junctions with sharp transition interfaces (*41*). The necessary control of low 10^{15} cm^{-3} p-type doping for the $\underline{P}^+/\pi/\underline{N}^+$ structure has never been achieved in more than 20 years of research on HgCdTe development by MBE. Present technology limits p-type doping with As values down to ~10^{16} cm^{-3} and even this amount of doping is usually not obtained reproducibly. Our novel diffusion process allowed arsenic concentrations well below the present technology.

Figure 13 shows a Gaussian-like distribution of an arsenic-implanted arsenic (open circles) reaching a depth of 0.6 μm from the surface. Deep diffusion of arsenic is achieved after annealing under a very low partial pressure of Hg, as initially demonstrated by Wijewarnasuriya et al. (*13*). As an example, figure 13 shows the arsenic profile by secondary ion mass spectroscopy (SIMS) after 16 h of annealing at 300 °C under appropriate Hg partial pressure (solid circles). After deep diffusion, the arsenic depth reaches 5 μm. After the diffusion anneal, an activation anneal was conducted at 400 °C for 5 min under Hg saturated conditions, followed by a Hg vacancy annihilation anneal at 250 °C for 18–20 h under Hg saturated conditions. The alloy composition was not measured by SIMS, and the author is, therefore, not able to comment on Cd interdiffusion. An important condition of $\underline{P}^+$ region is that minority carrier concentration should be low; consequently, under reverse biases, electrons should not replenish from the $\underline{P}^+$ region to the p-absorbing layer.
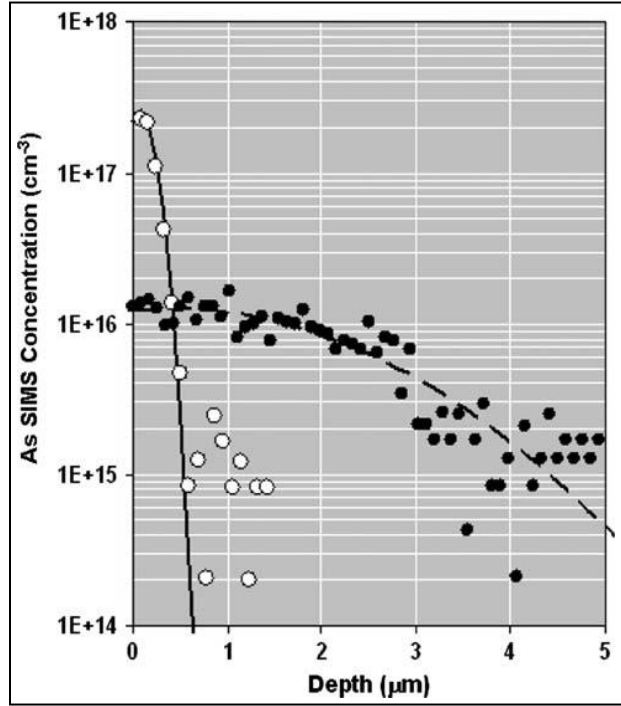
Figure 13. Typical example of arsenic redistribution from an arsenic-ion implanted source. Open symbols are as-implanted arsenic measured by SIMS and solid symbols show arsenic concentration after annealing at 300 °C under Hg diffusion conditions for 16 hours. Lines are Gaussian fits to the data.

The main parameters of variation are the anneal duration, Hg source temperature and corresponding Hg partial pressure P(Hg). All samples were held at 300 °C during the deep diffusion anneal. For each condition, the samples were sealed in a quartz ampoule and placed into a two-zone annealing apparatus, one zone for the samples and the other zone for the Hg source. The partial pressure of Hg was controlled by the Hg source temperature, and the corresponding pressure values were determined from a look-up table (*42*). Activation and vacancy annihilation anneals were carried out at 400 °C for 5 min and at 250 °C for 20 h, respectively. A 5 °C difference between the sample and Hg source was maintained to prevent condensation of Hg droplets on the sample surface during quenching. The As-diffusion profiles in the HgCdTe layers were measured by SIMS at Evans Analytical Group. As diffusion coefficients D(As) were then extracted from the profiles using a dopant distribution model, as described below (*43*):

$$C = \frac{Q}{\sqrt{\pi Dt}} \exp\left(-\frac{(d-R)^2}{4Dt}\right)$$

where, d is the depth from the sample surface, t is the annealing duration, Q is the implant dose, and R is the fitting parameters for peak depth.

20

The SIMS profiles for LWIR material annealed with varying Hg partial pressure are shown in figure 14.
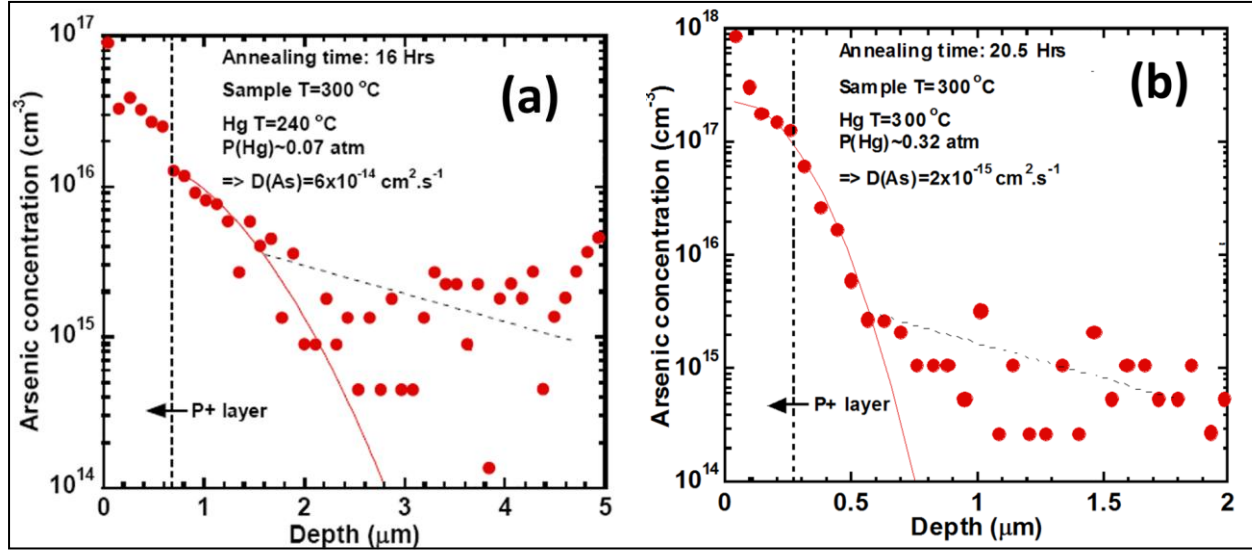
Figure 14. SIMS data of LWIR As diffusion profile for (a) 16 hour anneal at P(Hg) 0.07 atm and (b) 20.5 hour anneal at P(Hg) = 0.32 atm.

Comparing the junction depth of the $\underline{P}^+/\pi$ interface and the absorber region widths, deeper As diffusion is observed in the sample annealed under lower Hg pressure (0.07 atm). The data in figure 14a exhibits a junction depth of 2.5 μm, an absorber region between the depths of 1 μm and 5 μm, and an As doping concentration in the range of $10^{15} - 10^{16}$ cm^{-3}. The data in figure 14b exhibits a junction depth of 0.6 μm, an absorber region between 0.8 μm and 1.6 μm, and an As doping level in the range of $10^{16} - 10^{17}$ cm^{-3}. The As concentration in the absorber region is an order of magnitude lower for the sample annealed at a lower Hg pressure due to the increased diffusion of As atoms through a higher concentration of Hg vacancies. As diffusion coefficients of D(As) = 6×10^{-14} cm^{2}S^{-1} and D(As) = 2×10^{-15} cm^{2}S^{-1} are extracted for samples in figures 14a and 14b, respectively,

All samples exhibited consistent $\underline{P}^+/\pi$ step-junction profiles with an arsenic concentration contrast of approximately two orders of magnitude in the $\underline{P}^+$ and π regions. We observe two primary components in the arsenic diffusion profiles: (1) a Gaussian component and (2) a linear component, as indicated in figure 15. These characteristics contribute to the $\underline{P}^+/\pi$ profile in which we are interested, As reported in past studies (*44*), the movement of As in HgCdTe during annealing can be described by fast and slow diffusion components. We believe the Gaussian distribution profile is attributed to the slower diffusion of arsenic atoms traveling primarily via Hg vacancies. We also believe that the linear tail of the profile may be a result of arsenic

channeling and possibly diffusion by means of other local defects associated with the ion implantation process.
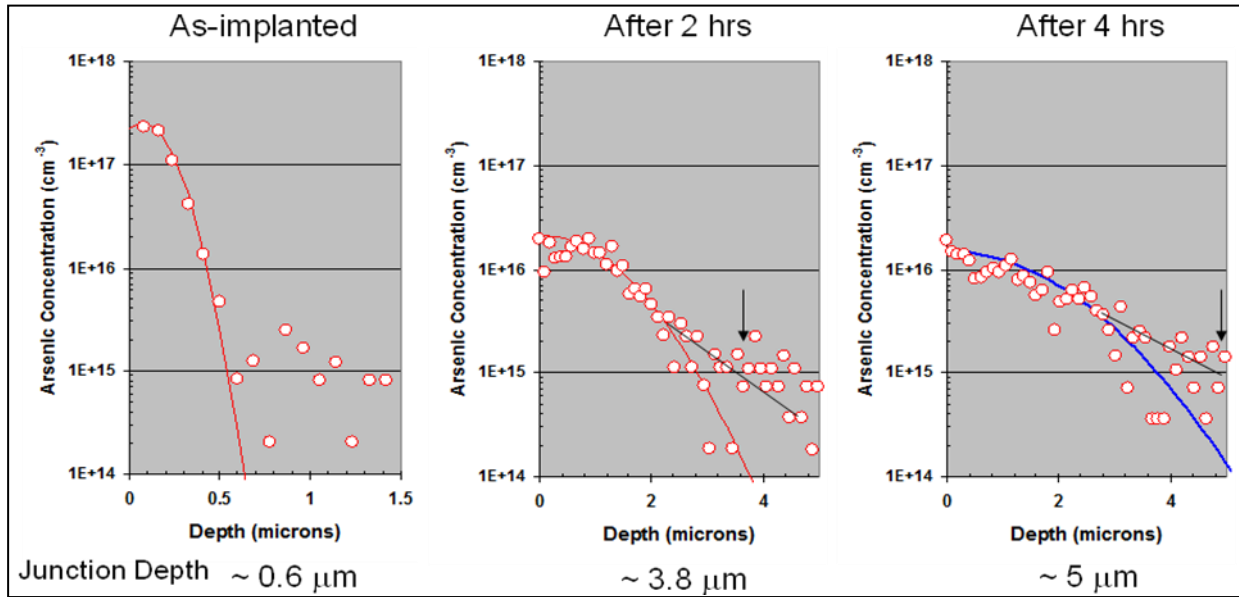
Figure 15. SIMS data of LWIR As diffusion profiles of as-implanted, after two hours, and after four hours of annealing at 300 °C under Hg-deficient condition. Obtained $D(As) = 9 \times 10^{-13}$ cm^{2}S^{-1}.

Our diffusion coefficients follow the general trend of the inverse relationship between the arsenic diffusion coefficient and the Hg partial pressure as described in past diffusion experiments (*45–47*). Figure 16 compares our extracted diffusion coefficients against values obtained in past studies.
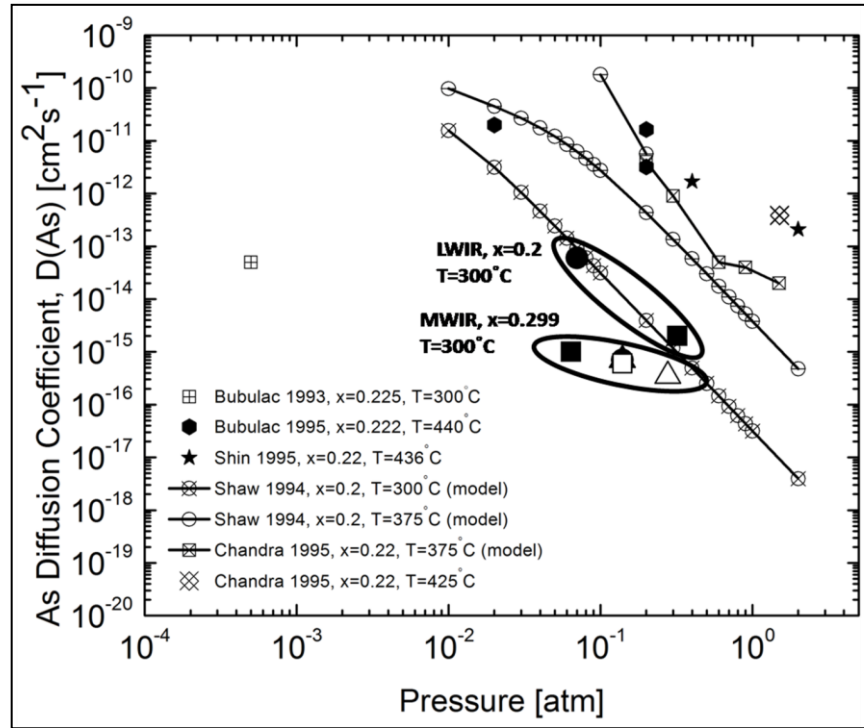
Figure 16. Published arsenic diffusion coefficient in HgCdTe.

It is important to note that our data points correspond to MBE-grown LWIR samples annealed at a low substrate temperature of 300 °C and longer annealing times, while most of the past studies focused on LWIR samples grown by MOCVD and LPE methods and annealed for short durations at higher substrate temperatures. We notice there is a difference in the diffusion coefficients we obtained for the LWIR samples. Comparing our LWIR diffusion coefficients for samples annealed at 300 °C to those projected by the diffusion coefficient model proposed for $Hg_{0.8}Cd_{0.2}Te$ by Shaw et al. (48) for the same temperature, we observe that our data points lie close to the model. Slight differences in the D(As) values may correspond primarily to non-idealities introduced by the actual experiment. Further studies need to be done to compare the diffusion coefficients of LWIR samples annealed at lower substrate temperatures to existing diffusion coefficient models.

A critical aspect of our novel diffusion process is the ability to maintain a good HgCdTe surface even after successful deep diffusion of As using a low Hg partial pressure. Several experiments were also carried out under different Hg pressures to optimize the surface smoothness of the HgCdTe surface before and after annealing. Figure 17 shows the surface under optimized arsenic deep diffusion conditions before and after annealing. The HgCdTe surface will become rough if the arsenic diffusion anneals conditions are not optimized, as shown in figure 18.

In order to take advantage of the higher minority carrier lifetime in p-type material, the absorber layer has to be lightly doped. This was achieved using our unique deep diffusion process at 300 °C, as indicated in figures 13 to 15. The doping concentration gradient in region II also helps to further diffuse electrons (in this case minority carriers in region II) to the p/$\underline{N}^+$ junction. The thickness of the absorber layer chosen in this case is about 5 μm, which is less than the diffusion length of minority electrons in region II. This is true even at ambient temperature, since the mobility of minority carriers (in these case electrons) is on the order of high 10^4 cm^2/V s and lifetime values are on the order of microseconds.
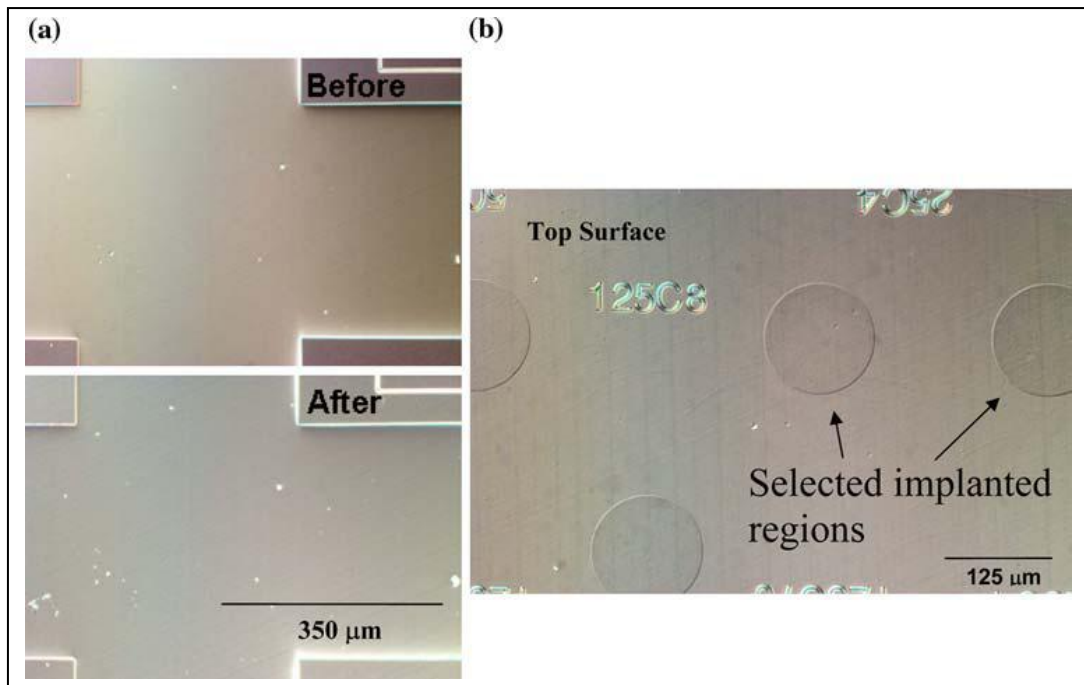

Figure 17. (a) Surface morphology under Normaski microscopy before and after diffusion anneals and (b) showing implanted regions under Normaski after complete anneals.
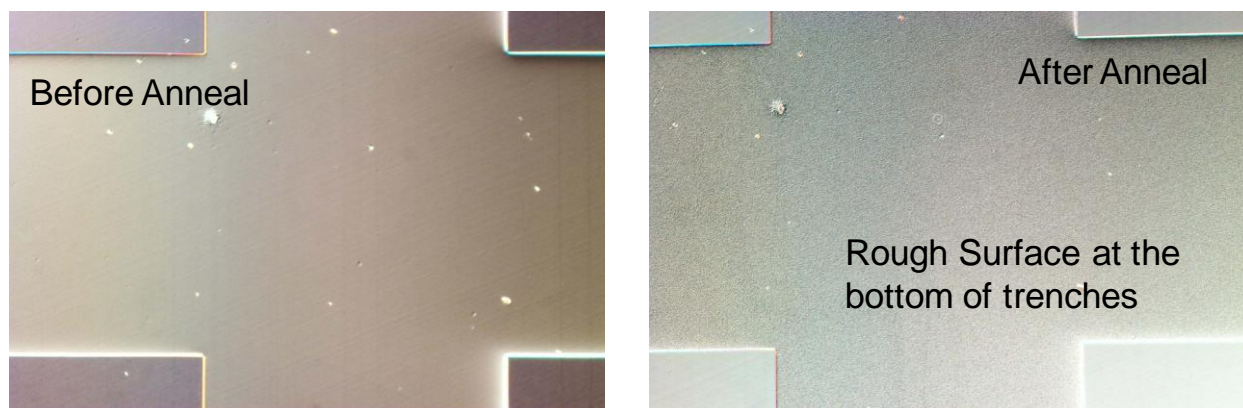
Figure 18. Surface morphology of the trenches under Normaski microscopy before and after diffusion anneals.

6. Current-Voltage Characteristics

I–V measurements were made from biases between –1000 mV and 0 mV. These measurements were made using a HP parameter analyzer. Figure 19 shows such I-V measurements on three 250 μm-diameter devices at 300 K. When the reverse bias increases, a sudden drop in the reverse current is observed. This sudden drop is attributed to Auger suppression and is due to the removal of the electrons in region II. As the electrons are removed from region II, hole concentrations are also reduced below the equilibrium value in order to maintain the charge balance. Hence, one of the critical interfaces of this type of architecture is the $\underline{P}^+$/p excluding interface. Leakage currents associated with electron replenishing at this interface are one of the major sources of high currents at ambient temperatures. A slightly modified architecture has been proposed to surmount this situation (*38*). At the transition voltage point, the devices exhibit infinite impedance. From the two measured devices, a relatively small spread in currents can be observed, indicating good uniformity in doping and material characteristics. These I–V curves show leakage currents with no soft breakdown characteristics in the high reverse-bias region, further indicating good-quality MBE material and fabrication process. An approximately 50% reduction in reverse current at high biases is shown in the figure. As indicated in the introduction, the main limitation of this structure is the leakage of electrons from the $\underline{P}^+$ to the p-region. An approximately 50% reduction in Auger suppression is seen, using Ag as a p-type dopant in a similar structure grown by MBE (*12*), and our present work also indicates about a 50% reduction at 300 K.

To assess the mechanisms controlling the device, I-V characteristics were measured on device as a function of temperature down to 130 K. As seen in figure 20, this device exhibited negative resistance characteristics from 300 K down to 130 K. Figure 19 shows the ratio of I_{max} to I_{min} as a

25

function of temperature. At ambient temperatures, the ratio tends to saturate at 2. A similar trend was observed in MOVPE grown structures by Elliott and co-workers (*6–8*).
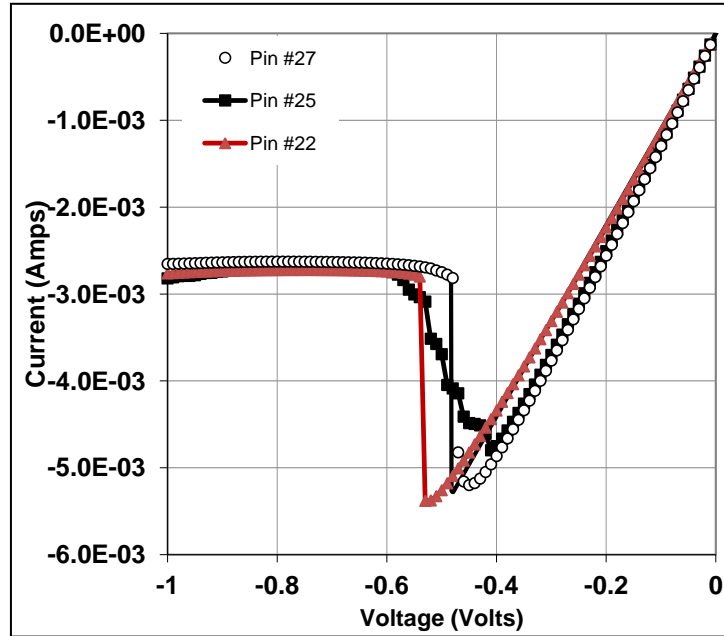

Figure 19. Measured current voltage characteristics at 300 K showing I_{Max}, I_{Min} and negative resistance region which resulted from suppression of Auger recombination.

NOTE: At high negative biases (away from negative resistance region) measured current is independent of applied bias indicating negligible tunneling currents. Calculated series resistance from the slope closer to zero bias is 78 Ohms. Device area is $A_j = 4.9 \times 10^{-4}$ cm^2. One of the two measured device at 300 K showing a steep transition from I_{Max} to I_{Min} in the reverse bias (solid triangular symbol). It is not well understood why some devices show a sharp transition and some devices show a soft transition from I_{Max} to I_{Min}.

Spectral response versus wavelength was measured under backside-illuminated conditions on the device. Figure 21 shows the response versus wavelength on the device at 100 K. The measured cut-off wavelength, λ_c, is approximately 10 µm at 100 K. The calculated response per photon versus wavelength is also displayed in figure 21 and can be seen to be near-classical behavior. The slight drop in response at shorter wavelengths is attributed to the interface recombination on the $\underline{N}^+$ layer. The detectors are non-antireflection coated at the back of the CdZnTe substrate and, hence, approximately 22% absorption is lost to reflection losses. The measured QE at –0.1 V at 7 µm wavelength is 0.54 at 100 K, which indicates the excellent quality of the HgCdTe. Softness of the response close to the cut-off wavelength region is due to the insufficient absorption due to the short absorber layer thickness.

At 100 K, this device showed contact issues due to less than desired p-type doping at the top contact (see figure 13). This is confirmed by the measured low QE at zero bias at 100 K. We have also measured response at 250 K (figure 22) and a near classical response was observed. This indicates that diffusion or collection lengths are larger than the absorber layer thickness. At 250 K, the diffusion length is expected to be lower than at 100 K, making it, therefore, surprising that there is a signal even at ambient temperatures such as 250 K. The measured cut-off is approximately 7.4 µm at 250 K (figure 23).
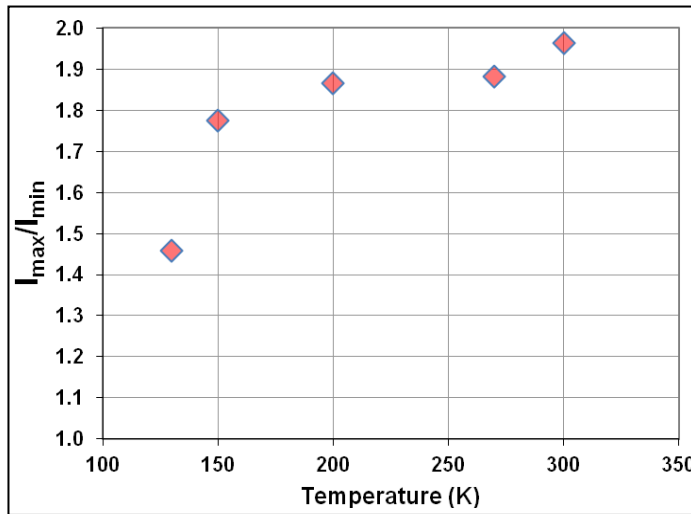
Figure 20. Measured ratio of I_{max} to I_{min} as a function of temperature.
The ratio reaches ~2 at 300 K.
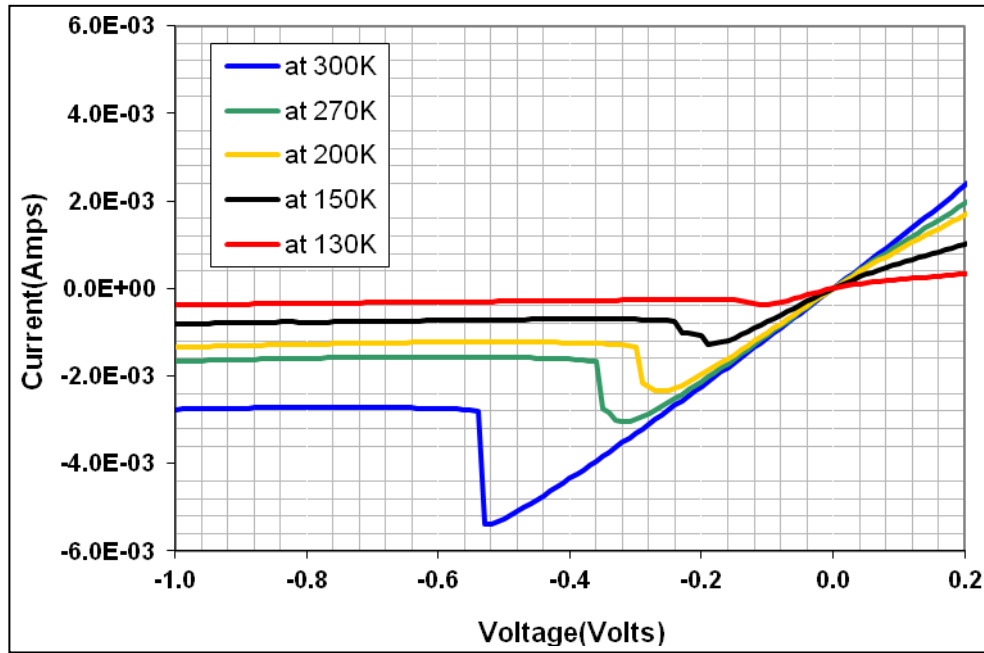
Figure 21. Measured current–voltage versus temperature characteristics of the device (see text) indicating negative differential resistance down to 130 K.
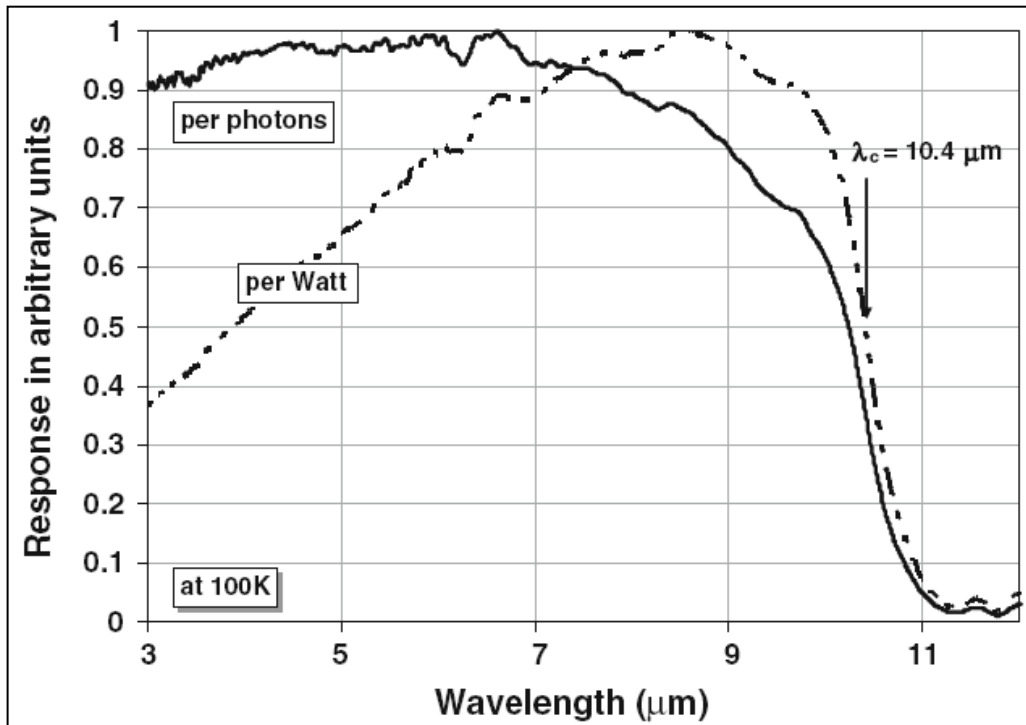
Figure 22. Measured spectral response versus wavelength at 100 K for a 250-μm-diameter device.
Both spectral responses, per photon and per Watt, show near-classical behavior.

NOTE: A slightly reduced response at shorter wavelengths is indicative of some surface recombination at the back interface. The obtained cut-off (λ_c) is 10.4 μm at 100 K. The cut-off is defined as the 50% spectral response point from the peak wavelength. The measured non-antireflective- coated device quantum efficiency at –0.1 V is 0.57 at a wavelength of 7 μm. The measured quantum efficiency at zero bias showed contact issues due to a less than desired p-type doping concentration at the top contact (see figure 13).
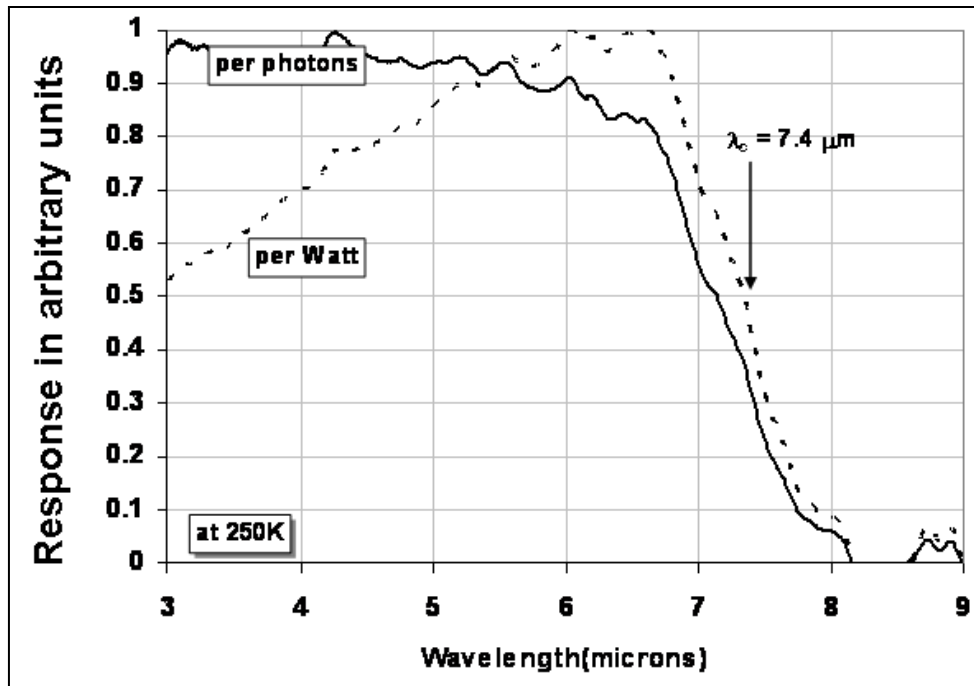
Figure 23. Measured spectral response versus wavelength at 250 K for a 250-µm-diameter device. Both spectral responses, per photon and per Watt, show near-classical behavior. The soft transition close to the cut-off is due to insufficient absorption due to the 5 µm thin p-layer. The obtained cut-off (λ_c) is 7.4 µm at 250 K.

7. Fitting Methodology

Steady-state numerical simulations are performed using Sentaurus Device, a commercial package by Synopsys (*49*). Sentaurus Device self-consistently determines a full coupled solution of the Poisson's equation and the continuity equations for electrons and holes using an approximate Newton method with Gaussian elimination. Fermi-Dirac statistics are used. HgCdTe material and recombination parameters—considering Auger, radiative and SRH recombination—are included in the model. Carrier degeneracy and conduction band non-parabolicity are also taken into account. Surface recombination and tunneling mechanisms are not accounted for in the simulations. Simulation output calculations of electrical and optical characteristics of HgCdTe p-n infrared photodiodes are comparable with published experimental data from different sources for long-wave infrared (LWIR) (*50*). The Cd alloy profile, including compositional grading at the two junctions, is taken from experimentally measured spectroscopic ellipsometry (SE) data and included in the simulation using a linear interpolation of the HgCdTe material parameters.

The calculated energy band diagram for this device at 1 V reverse bias and T=300 K is shown in figure 24a. Partial depletion of the absorber layer is achieved by increasing the reverse bias (depletion width is ~2–2.5 μm). The calculated equilibrium and non-equilibrium (1 V reverse bias) carrier concentration is shown in figure 24b. Under equilibrium, the LWIR absorber layer is essentially intrinsic. As the reverse bias is increased, the electron and hole concentration decreases by several orders of magnitude due to the effect of the exclusion/extraction layers. The hole concentration decreases down to the extrinsic p-type doping level for a depth <4 μm (non-depleted region). This initial simulation confirms that the NDR observed experimentally is likely due to strong Auger suppression in the device.
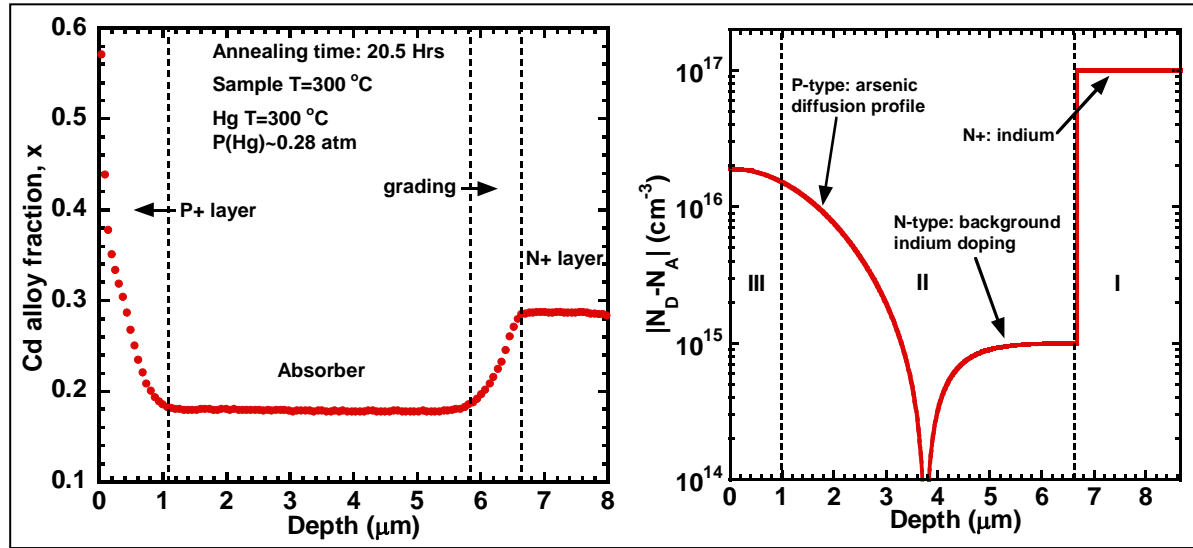
Figure 24. (a) Planar device structure, (b) Cd alloy composition after annealing obtained by SIMS, and (c) doping profile in the HOT structure.

Our device model is used to fit the temperature-dependent current-voltage data of HOT #42 shown in figure 19. We perform a 1D simulation of a cross-section of the device. In order to fit the I-V data for each temperature (120 K, 130 K, 150 K, 200 K, 270 K, and 300 K), we fit the maximum leakage current experimental value before Auger suppression (J_{max}) and the minimum leakage current experimental value after Auger suppression (J_{min}) as illustrated in figure 19. In our model, J_{min} is taken as the calculated current density at 500 mV reverse bias, which is found to be high enough for dark current saturation (neglecting the series resistance). J_{max} is taken as the maximum calculated current density between zero bias and 500 mV reverse bias. The temperature-dependent experimental values for J_{min} and J_{max} that we are fitting are shown in figure 19, along with the corresponding experimental reverse bias value.

Based on figure 24b, we set the Cd alloy composition profile in the top $\underline{P}^+$ layer, x(III), as a fitting parameter in the form of a linear grading $x_{top} \rightarrow 0.3$ (with $x_{top} > 0.3$). The two other fitting parameters are the ones that are found to have the most influence on the calculated device

characteristics: $|F_1F_2|$ in the absorber layer, which is related to the magnitude of Auger-1 processes and the SRH characteristic lifetime $\tau_{n0} = \tau_{p0}$ (assuming the same for electrons and holes) in the absorber layer, which is related to the concentration of traps, impurities, dislocations, or other elements causing SRH recombination, as well as their capture cross-sections. We observe that $|F_1F_2|$ mostly has an influence on the value of $(J_{max}-J_{min})$ and, therefore, the strength of the NDR. The SRH lifetime τ_{n0} (τ_{p0}) has an influence on the values of both J_{min} and J_{max}, but mostly on J_{min}. Table 2 summarizes the parameters used in our device model to fit the experimental I-V characteristics. In this case, the temperature dependence of $|F_1F_2|$ and τ_{n0} (τ_{p0}) is taken into account. The Cd alloy profile in the top $\underline{P}^+$ layer x(III) is constant with temperature. The doping profile and device geometry are taken from experimental data and designed values. Compositional grading between each region interface is taken into account. An iteration scheme described in details elsewhere is used to obtain the best values for each fitting parameter. The fitting for each temperature is obtained after a maximum of 2–3 iterations.

Ultimately, the goal of this fitting is to understand what mechanisms are limiting the leakage current just before (J_{max}) and after (J_{min}) Auger suppression. The total leakage current J_{tot} can be expressed as the sum of the electron diffusion current in the top $\underline{P}^+$ layer, $J_{n,diff}(\underline{P}^+)$, the hole diffusion current in the bottom $\underline{N}^+$ layer, $J_{p,diff}(\underline{N}^+)$, and the absorber layer current J_{abs}:

$$J_{tot} = J_{n,diff}\left(P^+\right) + J_{abs} + J_{p,diff}\left(N^+\right).$$

Table 2. Extracted fitting parameters.

T (K)	$|F_1F_2|$	$\tau_{n0}=\tau_{p0}$ (s)	J_{max} (A/cm^2)		J_{min} (A/cm^2)	
			Exp.	Sim.	Exp.	Sim.
120	0.29	2.8×10^{-7}	0.24	0.24	0.22	0.21
130	0.28	3.3×10^{-7}	0.76	0.75	0.52	0.51
150	0.26	3.7×10^{-7}	2.60	2.51	1.42	1.49
200	0.25	3.8×10^{-7}	4.78	4.85	2.49	2.41
270	0.21	3.5×10^{-7}	6.19	6.12	3.19	3.21
300	0.20	3.4×10^{-7}	10.96	10.83	5.54	5.52

As seen in figure 9, the absorber layer current is a combination of diffusion and g-r current, depending on the reverse bias. However, it is much more interesting to define it as the sum of an Auger-1 current in the absorber, J_{A1}, an Auger-7 current in the absorber, J_{A7}, and an SRH current in the absorber, J_{SRH}:

$$J_{abs} = J_{A1} + J_{A7} + J_{SRH}.$$

This way, we can determine the recombination mechanisms limiting the leakage current in the HgCdTe HOT photodiodes. J_{min} and J_{max} are fitted at each temperature using the set of three fitting parameters described earlier, and we extract from our simulation calculations the corresponding value for each current component mentioned in these last two equations. The values for the Auger and SRH currents in the absorber are determined by switching "on" and "off" each recombination mechanism separately in our device model.

Figure 25a shows the calculated magnitude of J_{max} after fitting, along with the various magnitudes of the leakage current components. According to our fitting result, the maximum current before Auger suppression, J_{max}, is limited by a SRH current in the absorber at T=120 K. This SRH current obtained in our model may be associated in the experimental device with a background trap concentration introduced during growth and/or processing. This SRH current has a weak dependence with temperature. We point out that, according to our model, SRH recombination is the limiting mechanism for J_{max} up to ~130–140 K. At T=120 K, both Auger-1 and Auger-7 currents in the absorber are very low compared to J_{SRH} because the intrinsic carrier concentration in the absorber is still relatively low. However, both currents rapidly increase as the temperature is increased. The Auger-1 current in the absorber limits J_{max} above ~130–140 K. Finally, the hole diffusion current in the bottom $\underline{N}^+$ layer stays relatively weak at all temperatures. The electron diffusion current in the top $\underline{P}^+$ layer has some influence on J_{max} above 270 K. Figure 25b shows the calculated magnitude of J_{min} after fitting, along with the different magnitudes of the leakage current components. According to our fitting results, the maximum current after Auger suppression (and before tunneling processes), J_{min}, is limited by a SRH current in the absorber between 120 K and room temperature. This is expected in LWIR HgCdTe and can be reduced as the HgCdTe growth and processing technology is further optimized. The Auger-1 current J_{A1}, which was found to limit J_{max} in figure 25a, is fully suppressed as the reverse bias is increased and is, therefore, not shown in figure 25b. The Auger-7 current in the absorber J_{A7} increases as the temperature is increased. Although it is not found to limit J_{min}, it shows that the Auger-7 current is only partially suppressed in the device. **The amount of Auger-7 suppression is ~70 % according to our results**. The hole diffusion current in the bottom $\underline{N}^+$ layer stays relatively weak at all temperatures, as observed when analyzing J_{max}. The electron diffusion current in the top $\underline{P}^+$ layer has some influence on J_{min} above 270 K. This analysis gives us significant insight on the limiting leakage current mechanisms in experimental LWIR HOT devices, both before and after Auger suppression. Dark current caused by tunneling mechanisms is expected to occur at higher biases than the one considered here and is, consequently, not observed in our simulations.

The saturation current in our experimental device (J_{min}) is next compared to that in a standard HgCdTe DLPH photodiode simulated using our device model. We also compare J_{min} to the dark current in a simulated ideal HOT photodiode with the same fixed cutoff wavelength as the experimental device (~10.4 μm at 100 K). We plot the dark current at 200 mV reverse bias

33

versus T using our numerical model for ideal HOT and DLPH photodiodes (x(abs)=0.22), characterized by a low n-type doping in the absorber, N_D(absorber)= 1×10^{15} cm^{-3}, and a much longer $\tau_{n0}=\tau_{n0}=5$ μs than what we observed experimentally. As seen in figure 26, the fabricated HOT device gives a lower saturation current J_{min} than for the ideal DLPH at all temperatures. Above ~200 K, both ideal and experimental HOT devices have comparable dark currents. Below 200 K, the experimental HOT device has a much larger saturation current than the ideal HOT device, which shows the room for improvement that can be achieved by optimizing the growth and fabrication process. Improvements are especially needed in terms of lower doping levels in the absorber layer and fewer traps/dislocations causing SRH recombination. At 300 K, factor of ~10 lower current density can be achieved with this non-equilibrium mode of operation by using low p-type doped in the absorber layer.


(a)   (b)
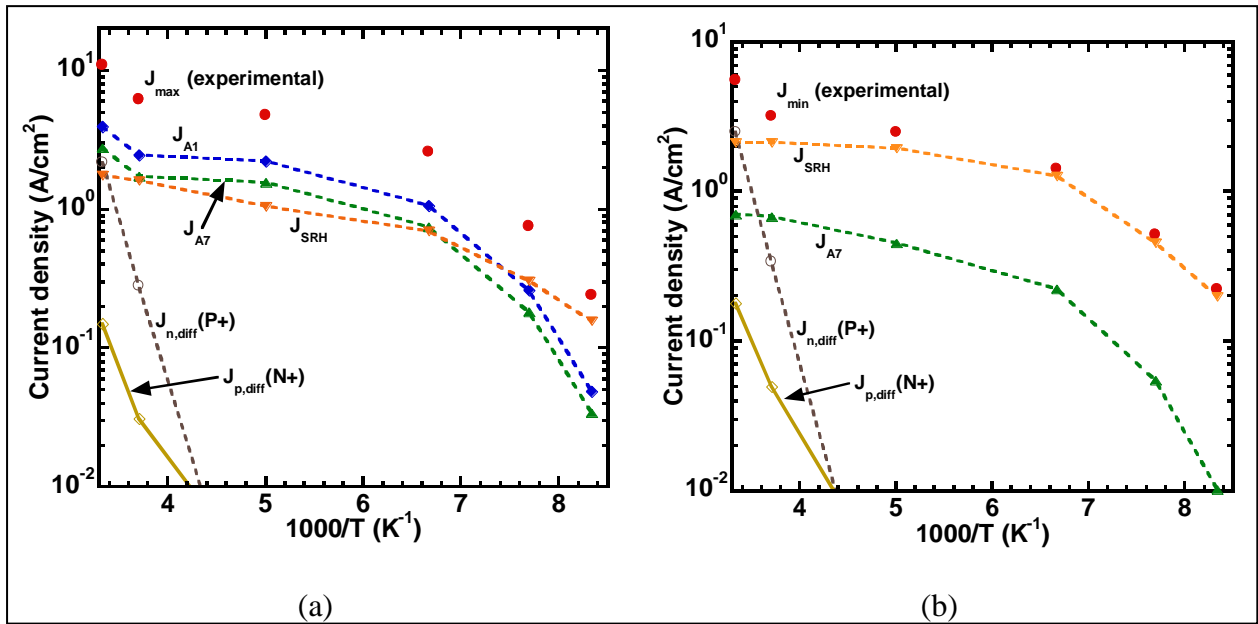
Figure 25. (a) Experimental values for J_{max} versus temperature. Also shown are the calculated Auger-1 current in the absorber J_{A1}, Auger-7 current in the absorber J_{A7}, SRH current in the absorber J_{SRH}, electron diffusion current in the top $\underline{P}^+$ layer $J_{n,diff}(\underline{P}^+)$, and hole diffusion current in the bottom $\underline{N}^+$ layer $J_{p,diff}(\underline{N}^+)$.
(b) Experimental values for J_{min} versus temperature. Also shown are the Auger-7 current in the absorber J_{A7}, SRH current in the absorber J_{SRH}, electron diffusion current in the top $\underline{P}^+$ layer $J_{n,diff}(\underline{P}^+)$, and hole diffusion current in the bottom $\underline{N}^+$ layer $J_{p,diff}(\underline{N}^+)$
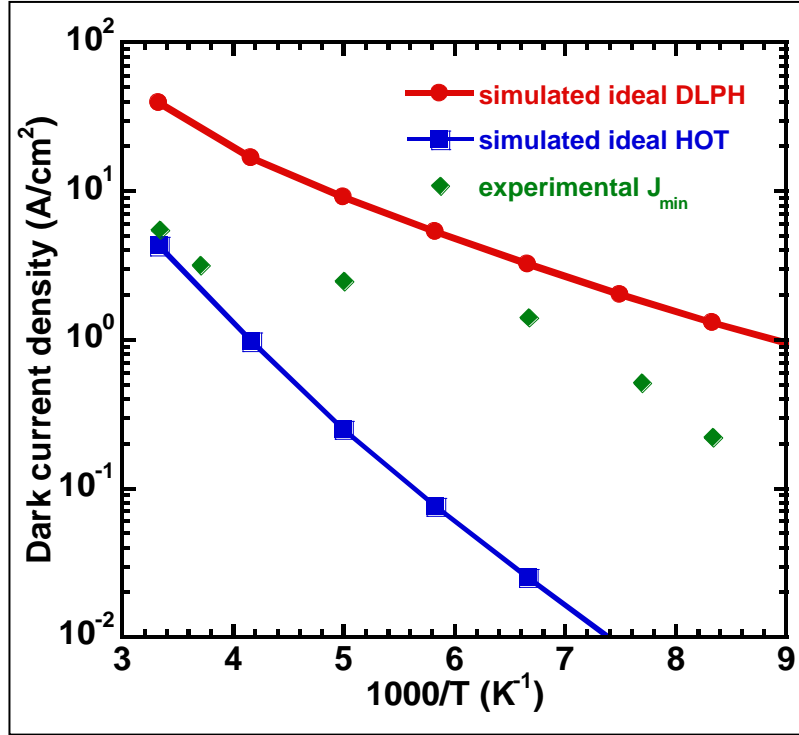
Figure 26. Calculated dark current density at 200 mV reverse bias for an ideal DLPH and HOT devices (with x(abs)=0.22) and experimental J_{min} versus temperature.

8. Conclusion

We have demonstrated Auger suppression devices at room temperature on p-type As doped LW-HgCdTe materials grown by MBE. We employed a three-layer device architecture $\underline{P}^+/\pi/\underline{N}^+$ in this work. Data shows about a 50% reduction in dark current is achieved at 300 K. A principal challenge was to obtain low p-type doping levels in the π-region. This issue was overcome using a novel, deep diffusion process, thereby demonstrating a successfully low-doped p-type HgCdTe in MBE grown material. Results indicate Auger suppression in $\underline{P}^+/\pi/\underline{N}^+$ devices above 130 K and the obtained saturation current is of the order of 5 A/cm^2 on these devices at 300 K. The threshold voltage is 450 mV at 300 K and 100 mV at 130 K for 250-micron circular devices. Results show reducing the series resistance could reduce this further. Near-classical spectral responses were obtained at 250 K and 100 K. Measured non-AR QE at 100 K was 0.57. By fitting the temperature-dependent current-voltage experimental data for one selected device where clear NDR is observed, we confirmed that the NDR is due to Auger suppression. More specifically, NDR is attributed to full suppression of Auger-1 processes and partial suppression of Auger-7 processes. The percentage of Auger-7 suppression is ~70 %. After Auger

suppression, the remaining leakage current is mostly limited by a high SRH recombination component in these devices.

Also in this study, we have demonstrated a novel method of shallow arsenic ion implantation and deep diffusion anneal to obtain controllable deep diffusion of low arsenic concentrations in MBE grown HgCdTe DLPH samples, while retaining the $\underline{P}^+/\pi$ step structure, We achieved low arsenic concentrations of (0.8 to 2)$\times 10^{15}$ cm^{-3} in the absorber region using low Hg partial pressure and long anneal times, Finally, we discussed the behavior of arsenic in HgCdTe as a function of variations in the deep diffusion parameters,

9. References

1. Ashley, T.; Elliott, C. T.; Harker, A. T. *Infrared Phys.* **1986**, *26*, 303.

2. Kinch, M. A.; Aqariden, F.; Chandra, D.; Liao, P-K.; Schaake, H. F.; Shih, H. D. *J Electron. Mater.* **2007**, *34*, 880 and Kinch, M. A. *Fundamentals of Infrared Detector Materials*, SPIE Press, Vol. TT76 (2007).

3. Kozlowski, L. J.; Vural, K.; Luo, J.; Tomasini, A.; Liu, T.; Kleinhans, W. E. Low-Noise Infrared and Visible Focal Plane Arrays. *Opto-Electronics Review* **1999**, *7*, 259–269.

4. Wijewarnasuriya, P. S.; Zandian, M.; Young, D. B.; Waldrop, J.; Edwall, D. D.; McLevige, W. V.; Lee, D.; Arias, J.; D'Souza, A. I. Microscopic Defects on MBE Grown LWIR $Hg_{1-x}Cd_xTe$ Material and Their Impact on Device Performance. *J. Electron. Mater.* **Jun. 1999**, *28* (6), 649–653.

5. Dhar, N. K. DARPA Broad Agency Announcement, DARPA-BAA-08-64.

6. Ashley, T.; Elliott, C. T.; Harker, A. T. *Infrared Phys.* **1986**, *26*, 303.

7. Ashley, T.; Elliott, C. T. *Electron. Lett.* **1985**, *21*, 451.

8. Elliott, C. T.; Gordon, N. T.; Hall, R. S.; Phillips, T. J.; White, A. M.; Jones, C. L.; Maxey, C. D.; Metcalfe, N. E. *J. Electron. Mater.* **1996**, *25*, 1139.

9. Wu, O. K.; Kamath, G. S.; Redford, W. A.; Bratt, P. R.; Patten, E. A. *J. Vac. Sci. Technol.* **1990**, *A8*, 1034.

10. Wijewarnasuriya, P. S.; Sivananthan, S. *Appl. Phys. Lett.* **1998**, *72*, 1694.

11. Capper, P. *J. Vac. Sci. Technol.* **1991**, *B9*, 1667.

12. Skauli, T.; Steen, H.; Colin, T.; Helgesen, P.; Lovold, S.; Elliott, C. T.; Gordon, N. T.; Phillips, T. J.; White, A. M. *Appl. Phys. Lett.* **1996**, *68*, 1235.

13. Wijewarnasuriya, P. S.; Emelie, P. Y.; D'Souza, A.; Brill, G.; Stapelbroek, A. G.; Velicu S.; Chen, Y.; Grein, C.; Sivananthan, S.; Dhar, N. K. *J. Electron. Mater.* **2008**, *37*, 1283.

14. Blakemore, J. S. Semiconductor Statistics (Pergamon, New York, 1962).

15. Pratt, R. G.; Hewett, J.; Capper, P.; Jones, C. L.; Quelch, M. J. *J. Appl. Phys.* **1983**, *54*, 5122.

16. Kinch, M. A.; Brau, M. J.; Simmons, A. *J. Appl. Phys.* **1973**, *44*, 1649.

17. Casselman, T. N. Proc. Fourth Intern. Conf. On Physics of Narrow Gap Semiconductors, Linz, Austria, 1981 pub. By Springer Verlag, Berlin (1982), p. 147 (Lecture Notes on Physics, Vol. **152**).

18. Peterson, P. E. *J. Appl. Phys.* **1970**, *41*, 3465.

19. Lopes, V. C.; Syllaios, A. J.; Chen, M. C. *Semicond. Sci. Technol.* **1993**, *8*, 824.

20. Wijewarnasuriya, P. S.; Lange, M. D.; Sivananthan, S.; Faurie, J. P. *J. Appl. Phys.* **1994**, *75*, 1005.

21. Wijewarnasuriya, P. S.; Lange, M. D.; Sivananthan, S.; Faurie, J. P. *J. Elect. Mat.* **1995**, *24*, 545.

22. de Souza, M. E.; Boukerche, M.; Faurie, J. P. *J. Appl. Phys.* **1990**, *68*, 5195.

23. Edwall, D. D.; Zandian, M.; Chen, A. C.; Arias, J. M. *J. Elect. Mat.*

24. Beattie, A. R. *Semicond. Sci. Technol.* **1987**, *2*, 281.

25. Capper, P. *J. Crystal Growth* **1982**, *57*, 280.

26. Jones, C. L. Properties of Mercury Cadmium Telluride ed J. Brice and P. capper (New York: INSPEC) p. 137 (1987).

27. Baryshew, N. S.; Gelmont, B. L.; Ibragimova, M. J. *Sov. Phys. Semocond.* **1990**, *24*, 127.

28. Hansen, G. L.; Schmit, J. L.; Casselman, T. N. *J. Appl. Phys.* **1982,** *53*, 7099.

29. Blue, M. D. *Phys. Rev.* **1964**, *134*, A226.

30. Streetman, B. G. *Solid State Electronic Devices*, 1980, Prentice-Hall, Inc. Englewood Cliffs, New Jersey, 07632

31. Sze, S. M. *Physics of Semiconductor Devices*, Second Edition, Pg. 92, 1981, John Wiley & Sons, Inc. New York

32. Shockley,W. *Electrons and Holes in Semiconductors*, D. Van Nostrand, Princeton, New Jersey, 1950.

33. Nemirovsky, Y.; Rosenfeld, D.; Adar, R.; Kornfeld, A. *J. Vac. Sci. Tech.* **1989**, *A 7*, 528.

34. Reine, M. B.; Tredwell, T. J.; Sood, A. K. *Photovoltaic Infrared Detectors* chapter, Semiconductors and Semimetals **Vol. 18**, R. K. Willardson and A. C. Beer editors, Academic Press, NY, 1981.

35. Sze, S. M. *Physics of Semiconductor Devices*, p. 98 (John Wiley & Sons, 1981).

36. Kinch, M. A. *J. Vac. Sci. Technol.* **1982**, *21*, 215.

37. Humphreys, R. G. *Infrared Phys.* **1986**, *26*, 337.

38. Elliott, C. T. *Proc. SPIE* **1996**, *2744*, 452.

39. Arias, J. M.; Pasko, J. G.; Zandian, M.; Shin, S. H.; Williams, G. M.; Bubulac, L. O.; DeWames, R. E.; Tennant, W. E. *J. Electron. Mater.* **1993**, *22*, 1049.

40. D'Souza, A. I.; Bajaj, J.; DeWames, R. E.; Edwell, D. D.; Wijewarnasuriya, P.; Nayer, N. *J. Electron. Mater.* **1998**, *27*, 727.

41. Capper, P, *J. Vac. Sci. Technol.* **1991**, *B9*, 1667.

42. Vydyanath, H. R.; Hiner, C. H. *J. Appl. Phys.* **1989**, *65*, 3080.

43. Crank, J. C. *The Mathematics of Diffusion*, Second Edition, Clarenden, Press, Oxford.

44. Bubulc, L. O.; Edwall, D. D.; Irvine, S.J.C.; Gertner, E. R.; Shin, S. H. *J. Elec. Mater.* **1995**, *24* (5), 617.

45. Shin, S. H.; Arias, J. M.; Zandian, M.; Pasko, J. G.; Bubulac, L. O.; De Wames, R. E. *J. Elec. Mater.* **1995**, *24* (5), 609.

46. Shaw, D. *J. Elec. Mater.* **1995**, *24* (5), 587.

47. Chandra, D.; Weirauch, D. F.; Schaake, H. F.; Kinch, M. A.; Aqariden, F.; Wan, C. F.; Shih, H. D. *J. Elec. Mater.* **2005**, *34*, 963.

48. Shaw, D. *Semicond. Sci. technol.* **1994**, *9*, 1729.

49. Sentaurus Device Manual, Synopsys (2005).

50. Velicu, S.; Grein, C. H.; Emelie, P. Y.; Itsuno, A.; Phillips, J. D.; Wijewarnasuriya, P. S. *Proc. Of SPIE*, Vol. 7608, 760820 (2010).

List of Symbols, Abbreviations, and Acronyms

Ag	silver
BLIP	background-limited performance
BTB	band-to-band
FTIR	Fourier transform infrared
g-r	generation-=recombination
HgCdTe	mercury cadmium telluride
HOT	high-operating-temperature
InSb	indium antimony
I-V	current-voltage
LWIR	long-wave infrared
MBE	molecular beam epitaxy
NDR	negative differential resistance
PEC	process evaluation chips
PV	photovoltaic
QE	quantum efficiency
SE	spectroscopic ellepsometry
SIMS	secondary ion mass spectroscopy
SRH	Shockley-Read-Hall
SWaP	size, weight and power
TAT	trap-assisted tunneling

INTENTIONALLY LEFT BLANK.